



Evolution of Primordial Magnetic Fields during Large-scale Structure Formation

Salome Mtchedlidze^{1,2,3} , Paola Domínguez-Fernández^{4,5} , Xiaolong Du⁶ , Axel Brandenburg^{1,7,8,9} ,
Tina Kahniashvili^{1,3,9,10} , Shane O’Sullivan¹¹ , Wolfram Schmidt⁴ , and Marcus Brüggen⁴

¹ School of Natural Sciences and Medicine, Ilia State University, 3-5 Cholokashvili St., 0194 Tbilisi, Georgia; salome.mtchedlidze.1@iliauni.edu

² Institut für Astrophysik, Georg-August-Universität Göttingen, Friedrich-Hund-Platz 1, D-37077 Göttingen, Germany

³ Abastumani Astrophysical Observatory, Tbilisi, GE-0179, Georgia

⁴ Hamburger Sternwarte, Universität Hamburg, Gojenbergsweg 112, D-21029 Hamburg, Germany

⁵ Department of Physics, School of Natural Sciences UNIST, Ulsan 44919, Republic of Korea

⁶ Carnegie Observatories, 813 Santa Barbara St., Pasadena, CA 91101, USA

⁷ Nordita, KTH Royal Institute of Technology and Stockholm University, Hannes Alfvéns väg 12, SE-10691 Stockholm, Sweden

⁸ The Oskar Klein Centre, Department of Astronomy, Stockholm University, AlbaNova, SE-10691 Stockholm, Sweden

⁹ McWilliams Center for Cosmology and Department of Physics, Carnegie Mellon University, 5000 Forbes Ave., Pittsburgh, PA 15213, USA

¹⁰ Department of Physics, Laurentian University, Ramsey Lake Rd., Sudbury, ON P3E 2C, Canada

¹¹ School of Physical Sciences and Centre for Astrophysics & Relativity, Dublin City University, Glasnevin, D09 W6Y4, Ireland

Received 2021 September 30; revised 2022 January 20; accepted 2022 February 25; published 2022 April 20

Abstract

Primordial magnetic fields (PMFs) could explain the large-scale magnetic fields present in the universe. Inflation and phase transitions in the early universe could give rise to such fields with unique characteristics. We investigate the magnetohydrodynamic evolution of these magnetogenesis scenarios with cosmological simulations. We evolve inflation-generated magnetic fields either as (i) uniform (homogeneous) or as (ii) scale-invariant stochastic fields, and phase-transition-generated ones either as (iii) helical or as (iv) nonhelical fields from the radiation-dominated epoch. We find that the final distribution of magnetic fields in the simulated cosmic web shows a dependence on the initial strength and the topology of the seed field. Thus, the observed field configuration retains information on the initial conditions at the moment of the field generation. If detected, PMF observations would open a new window for indirect probes of the early universe. The differences between the competing models are revealed on the scale of galaxy clusters, bridges, as well as filaments and voids. The distinctive spectral evolution of different seed fields produces imprints on the correlation length today. We discuss how the differences between rotation measures from highly ionized regions can potentially be probed with forthcoming surveys.

Unified Astronomy Thesaurus concepts: [Magnetohydrodynamical simulations \(1966\)](#); [Large-scale structure of the universe \(902\)](#); [Intergalactic medium \(813\)](#); [Primordial magnetic fields \(1294\)](#)

1. Introduction

Magnetic fields pervade the universe on different observable scales from planets and stars (e.g., Stevenson 2010; Schubert & Soderlund 2011) to galaxies and galaxy clusters (e.g., Beck 2001; Beck & Wiełebinski 2013). Different observational techniques reveal the large-scale morphology of these fields on galaxy and galaxy-cluster scales with microgauss strengths and correlation lengths reaching a few tens of kiloparsec in galaxy clusters (see, e.g., Murgia et al. 2004; Vogt & Enßlin 2005).

The existing theories for explaining such large-scale correlated magnetic fields can be broadly divided into two classes: (1) the primordial scenario, where a seed magnetic field is generated in the early universe, during epochs preceding structure formation (Kandus et al. 2011); and (2) the astrophysical scenario, where the observed magnetic fields have their origin in an initial weak seed field produced in astrophysical sources (e.g., stars or active galactic nuclei within (proto-)galaxies) due to local mechanisms (e.g., Biermann battery; see Biermann 1950), and then amplified and transferred to larger scales (Kulsrud & Zweibel 2008; Ryu et al. 2008). For instance, the Biermann battery mechanism can generate seed magnetic fields from an initially zero magnetic field in

cosmological shocks driven by the gravitational structure formation (Ryu et al. 1998) or in ionization fronts during the Epoch of Reionization (Subramanian et al. 1994; Gnedin 2000).¹² Yet, it remains unclear how efficiently magnetic field seeds can spread in the astrophysical scenario (see, e.g., Bertone et al. 2006 and Marinacci et al. 2015 for studies on galactic winds).

Studies of Faraday rotation measurements and MgII absorption lines (tracing halos of galaxies) have shown that microgauss magnetic fields were already present in Milky Way-type galaxies a few billion years after the Big Bang (e.g., Kronberg et al. 2008; Bernet et al. 2008, 2010). Moreover, observations of blazar spectra by the Fermi Gamma Ray Observatory indicate that cosmic voids can host weak 10^{-16} – 10^{-15} G magnetic fields (coherent on megaparsec scales), which favors a primordial scenario;¹³ see, e.g., Neronov & Vovk (2010) and Tavecchio et al. (2010) for pioneering studies and Vachaspati (2021) for a review and references therein; also see Arlen et al. (2014) for discussions of possible uncertainties in the measurements of blazar spectra, and Broderick et al. (2018) and Alves Batista et al. (2019) on the possible impacts of plasma instabilities.



Original content from this work may be used under the terms of the [Creative Commons Attribution 4.0 licence](#). Any further distribution of this work must maintain attribution to the author(s) and the title of the work, journal citation and DOI.

¹² The reader may also refer to the following recent works: Naoz & Narayan (2013), Garaldi et al. (2021), and Attia et al. (2021).

¹³ Blazar spectra measurements can also be used to constrain the volume-filling factor of extragalactic magnetic fields seeded by starburst galaxies or active galactic nuclei; see (Dolag et al. 2011).

Seed magnetic fields generated in the early universe (e.g., primordial magnetic fields, PMFs) through its stress–energy tensor induce scalar (density), vector (vorticity), and tensor (gravitational waves) perturbations (see Subramanian 2016 for a review) and through these perturbations may leave potentially observable traces. In particular, the PMF effects include additional large- and small-scale angular anisotropies in the cosmic microwave background (CMB) temperature and polarization (see Planck Collaboration et al. 2016, and references therein), and changes in the matter power spectrum (see Wasserman 1978, Kim et al. 1996, and Gopal & Sethi 2003 for seminal work; and Fedeli & Moscardini 2012, Kahniashvili et al. 2013, Sanati et al. 2020, and Katz et al. 2021 for recent studies). Furthermore, the dissipation of PMFs throughout the intergalactic medium (IGM) in the pre-recombination era leads to spectral distortions in the CMB (Jedamzik et al. 2000), while their dissipation in the post-recombination era changes the thermal state of the IGM and alters the reionization history of the universe (Jedamzik et al. 1998; Sethi & Subramanian 2005, 2009). The observational signatures of PMFs also include the effects on the CMB polarization plane rotation; the Faraday rotation (CMB birefringence; see, e.g., Ade et al. 2015; Minami & Komatsu 2020) and the effects on light-element abundances during the Big Bang nucleosynthesis (BBN); see, e.g., Yamazaki & Kusakabe (2012) and Luo et al. (2019). At high redshifts, PMFs are proposed to lower the angular momentum barrier of a collapsing gas leading to direct collapse black hole formation (Pandey et al. 2019). Interestingly, recently PMFs have also been considered as a potential possibility to relax the Hubble tension (Jedamzik & Pogosian 2020).

PMFs could come from different generation scenarios, including inflation and phase transitions¹⁴ (see Grasso & Rubinstein 2001; Durrer & Neronov 2013; Subramanian 2016, for reviews). Inflationary magnetogenesis assumes that vacuum fluctuations of an electromagnetic (or hypermagnetic) field give rise to a weak seed field which then grows (see Turner & Widrow 1988 and Ratra 1992 for pioneering work, and Sharma et al. 2017, 2018, Bamba et al. 2021, and Maity et al. 2021 for recent studies and references therein). This mechanism usually involves the breaking of the conformal invariance of spacetime (see, e.g., Dolgov 1993). The correlation lengths of inflation-generated magnetic fields are not limited by causality requirements due to rapid exponential stretching during inflation. On the other hand, a phase-transition mechanism implies that the coherence scales of the PMFs are bound due to causality by the Hubble horizon length scale at the moment of field generation, i.e., electroweak (EW, $T \sim 100$ GeV) or quantum-chromodynamical (QCD, $T \sim 150$ MeV) phase transitions; see Hogan (1983), Quashnock et al. (1989), Vachaspati (1991), and Tajima et al. (1992) for pioneering work, and Subramanian (2016) and Vachaspati (2021) for reviews. The magnetic fields from phase transitions are assumed to have a stochastic distribution with either a power-law or a sharply peaked magnetic power spectrum (where the peak or the characteristic length scale is set by the phase-transition bubble size; see, e.g., Kahniashvili et al. 2010), while the inflationary

mechanism can produce a stochastic magnetic field with a scale-invariant spectrum or a spatially uniform, homogeneous magnetic field (i.e., the Mukohyama 2016 model; see Brandenburg et al. 2020, and references therein). Both generation scenarios, inflationary and phase-transitional, could generate helical PMFs (see the seminal work of Cornwall 1997, and Vachaspati 2021 for a review and references therein). The relevance of a primordial, helical magnetic field is that, if ever detected, it will be a direct indication of parity (mirror symmetry) violation in the early universe and can in turn explain the matter–antimatter asymmetry (see Giovannini & Shaposhnikov 1998 and Vachaspati 2001 for pioneering work, and the recent work of Fujita & Kamada 2016 and Kushwaha & Shankaranarayanan 2021).

The current observational upper limits on the strength of PMFs are derived from CMB observations and depend on the specific effects that are analyzed. The effects of PMFs on the CMB angular power spectrum suggest a few nanogauss for the upper bound of the amplitude of stochastic PMFs (~ 4.4 nG assuming zero helicity and ~ 5.6 nG for a maximally helical field at a scale of 1 Mpc and with a power-law power spectrum; Planck Collaboration et al. 2016). The strongest upper limits on the PMF arise from the inhomogeneous recombination induced by small baryonic density perturbations (Jedamzik & Savelev 2019). On the other hand, the nonobservation of gigaelectronvolt photons from tera-electronvolt blazars puts a lower limit of order 10^{-15} – 10^{-16} G on the strength of the primordial magnetic seed characterized by a monochromatic spectrum, i.e., characterized by a fixed correlation length of 1 Mpc (Taylor et al. 2011).

PMFs are expected to evolve in a distinguishable fashion across different cosmological epochs. Their evolution has been widely studied in numerical simulations either with pure magnetohydrodynamical (MHD) codes (only for radiation-dominated epochs); see, e.g., Pouquet et al. (1976), Christensson et al. (2001), Banerjee & Jedamzik (2004), Kahniashvili et al. (2016), and Brandenburg et al. (2018); or, more recently, with cosmological MHD simulations (post-recombination epoch); see, e.g., Miniati & Beresnyak (2015), Beresnyak & Miniati (2016), Vazza et al. (2017), Vazza et al. (2018), and also Donnert et al. (2018) for a recent review. The evolution of PMFs in the radiation-dominated epoch, generated via the inflation and phase-transition mechanisms, proceeds in a highly turbulent regime due to the strong coupling between magnetic fields and plasma motions (Brandenburg & Nordlund 2011). It has been shown that freely decaying MHD turbulence with helicity could source energy cascades from small to larger scales and a slowdown of the decay (Christensson et al. 2001; Banerjee & Jedamzik 2004; Kahniashvili & Brandenburg 2010; Brandenburg & Kahniashvili 2017) leading to 10^{-15} – 10^{-9} G magnetic fields by the end of recombination (Kahniashvili et al. 2020). On the other hand, it is important to connect this work with cosmological simulations, which can reproduce the observed magnetization of the universe on larger scales (\sim megaparsec scales) and later stages (during structure formation), assuming either a primordial (Dolag et al. 1999; Brüggén et al. 2005; Vazza et al. 2014; Marinacci et al. 2015) or an astrophysical scenario with various mechanisms of magnetic seed transport (e.g., star formation and outflows from active galactic nuclei; Bertone et al. 2006; Donnert et al. 2009; Xu et al. 2011; Vazza et al. 2017). Regardless of their origin, the physical mechanisms that further amplify magnetic fields during cosmological structure formation are adiabatic contraction and

¹⁴ Generally, the topological defects arising from various phase transitions in the early universe could also source the generation of PMFs; see, e.g., Horiguchi et al. (2015) and a review on topological defects by Durrer et al. (2002). In addition, cosmic strings are another possible source of PMF generation (see Vachaspati 2021, for a review).

Table 1
Initial Conditions for the Magnetic Field^a

Scenario	Model	Normalization (nG)	Simulation ID	$\langle B_0^2 \rangle$ (nG ²)	$\langle B_0 \rangle$ (nG)	k_{peak} ($h \text{ Mpc}^{-1}$)	λ_{peak} ($h^{-1} \text{ Mpc}$)
Inflationary	(i) Uniform	0.1	u01	0.0072	0.085
		0.5	u05	0.180	0.390
		1	u1	0.719	0.804
	(ii) Scale-invariant	0.1	s01	0.0072	0.079	0.02	45
		0.5	s05	0.180	0.395	0.02	45
		1	s1	0.719	0.790	0.02	45
Phase-transitional	(iii) Helical	0.1	h01	0.0072	0.080	0.4	2.6
		0.5	h05	0.180	0.402	0.4	2.6
		1	h1	0.719	0.781	0.4	2.6
	(iv) Nonhelical	0.1	nh01	0.0072	0.085	0.8	1.26
		0.5	nh05	0.180	0.424	0.8	1.26
		1	nh1	0.719	0.848	0.8	1.26

Note.

^a We use comoving quantities everywhere unless stated otherwise. The characteristic wavenumber and scale of the magnetic spectra is denoted by k_{peak} and λ_{peak} accordingly, and $\langle B_0^2 \rangle$ and $\langle B_0 \rangle$ are the mean of the initial magnetic field energy and the initial magnetic field strength, respectively.

turbulent dynamo. The latter is the preferred mechanism for explaining the efficient amplification of magnetic fields on galaxy (see, e.g., Pakmor et al. 2017; Rieder & Teyssier 2017; Steinwandel et al. 2020) and galaxy-cluster scales (see, e.g., Xu et al. 2009; Vazza et al. 2018; Domínguez-Fernández et al. 2019; Steinwandel et al. 2021). Nevertheless, distinguishing between different magnetogenesis scenarios in the high-density regions of the cosmic web could be complicated because the memory of the seed field is believed to be erased by the turbulent dynamo (Cho 2014).¹⁵ This picture can change in the more rarefied regions of the cosmic web, such as cluster outskirts, filaments and voids, where competing models can be observationally tested (see, e.g., Donnert et al. 2009; Vazza et al. 2017).

In the present paper, the cosmological MHD simulations are performed with the Enzo code (Bryan et al. 2014), where the initial magnetic field seeding¹⁶ is consistent with different primordial magnetogenesis scenarios. For the first time, we compare the large-scale evolution of inflationary and phase-transitional magnetogenesis scenarios. We focused on studying two subcases for each scenario. In the inflationary case, we study (i) a uniform, homogeneous and (ii) a stochastic, scale-invariant initial magnetic field. In the phase-transitional case, we study (iii) a helical and (iv) a nonhelical initial magnetic field.

This paper is organized as follows. In Section 2 we describe the numerical scheme and initial conditions adopted in our work. In Section 3 we discuss the physical model, define the spectral characteristics of each magnetogenesis scenario, and discuss the physical motivations. In Section 4 we present our results, with caveats discussed in Section 5, and we summarize our work in Section 6.

2. Simulations

We use the cosmological Eulerian MHD code Enzo (Bryan et al. 2014) for simulating a comoving volume of ($67.7 h^{-1} \text{ Mpc}^3$) with a resolution of $132 h^{-1} \text{ kpc}$. We employed a static uniform grid of 512^3 cells with 512^3 dark matter (DM) particles, each of mass $m_{\text{DM}} = 2.53 \times 10^8 M_{\odot}$. We use the Dedner formulation of MHD equations that handles the divergence-free condition with a cleaning algorithm for magnetic monopoles (Dedner et al. 2002). The spatial reconstruction is done using the piecewise linear method (PLM; van Leer 1979; Colella & Glaz 1985) and fluxes at cell interfaces are calculated using the Harten–Lax–van Leer (HLL) Riemann solver (Toro 1997). The time integration is performed using the total variation diminishing second-order Runge–Kutta (RK) scheme (Shu & Osher 1988). We use the dual-energy formalism (DEF; Bryan et al. 1995) to avoid numerical instabilities in the regions with highly supersonic flows. Here we focus on the effects of magnetic amplification due to large-scale structure (LSS) formation. We therefore neglect radiative gas cooling, chemical evolution, star formation, and feedback from active galactic nuclei. While our resolution is not suited for studying structures inside collapsed objects, it is sufficient to capture the effects on the magnetic cosmic web. This is a first step in describing the evolution of more realistic PMFs than was done previously (using the uniform seed field; see, e.g., Marinacci et al. 2015; Vazza et al. 2014). We assume a Lambda cold dark matter (Λ CDM) cosmology (as in Planck Collaboration et al. 2020) with the following parameters: $h = 0.674$, $\Omega_m = 0.315$, $\Omega_b = 0.0493$, $\Omega_{\Lambda} = 0.685$, and $\sigma_8 = 0.807$.

2.1. Initial Conditions

We consider four different scenarios for the initial magnetic seed field (see Table 1 and Section 3 for the validity of the models):

1. Uniform (spatially homogeneous) field: we study an initial seed magnetic field with a constant strength across the whole computational domain. The magnetic field is directed

¹⁵ This is also the case in galaxies (see, e.g., Pakmor et al. 2014, Marinacci et al. 2015, Pillepich et al. 2018, and Arámburo-García et al. 2021 for cosmological simulations of galaxies).

¹⁶ Note that in general “seeding” refers to very weak magnetic fields at the moment of generation. However, hereinafter it will also refer to our initial conditions, where the magnetic field may not be very weak.

along the diagonal. This case corresponds to a particular inflationary magnetogenesis scenario, namely, the Mukohyama model (Mukohyama 2016).

2. Scale-invariant field: this is a setup for a stochastic, statistically homogeneous PMF with no helicity. This case corresponds to an inflationary scenario.¹⁷
3. Nonhelical field: a stochastic, phase-transitional PMF with no helicity.
4. Helical field: the same stochastic setup as (iii), but with helicity.

Any power-law decay/growth of the magnetic field and its correlation length on small scales is expected to virtually freeze at the end of the radiation-dominated epoch (Banerjee & Jedamzik 2004), while the large-scale evolution of PMFs during dark ages as well as after the reionization epoch is primarily dominated by the expansion of the universe (see Subramanian 2016, for a review).¹⁸ We initialize the simulation at $z = 50$ without loss of generality since no significant changes at the cosmological scales of interest for this work are expected between the recombination epoch and $z = 50$ redshift.

The seed magnetic field conditions (ii)–(iv) were reproduced with the PENCIL CODE (Pencil Code Collaboration et al. 2021). These were then used as initial conditions for the ENZO code. We normalized the mean magnetic energy density in all four cases (at initial redshift $z = 50$) to the same value corresponding to a mean (*effective*) magnetic field strength. The reader is referred to Appendix A for a detailed description of the generation of the initial magnetic conditions (ii)–(iv), including the setup for the helical field, as well as their normalization.

In Section 4.1, we discuss the results of three different normalizations: 0.1 nG, 0.5 nG, and 1 nG (see Table 1) for the uniform, scale-invariant, helical, and nonhelical models, respectively. In the remainder of the paper, we only discuss the results of the 1 nG normalization (which is below the upper limit from the CMB bounds; Planck Collaboration et al. 2016).

We show the initial magnetic power spectra for the stochastic setups considering a 1 nG normalization in Figure 1. The initial velocities and densities are generated according to the transfer function of Eisenstein & Hu (1998), which accounts for the evolution of (post-inflationary) linear perturbations but neglects any effects from PMFs. PMFs are expected to affect the initial density power spectrum and can produce additional clustering of matter on intermediate and small scales (Sethi & Subramanian 2005; Yamazaki et al. 2006; Fedeli & Moscardini 2012; Kahnashvili et al. 2013; Sanati et al. 2020). As was mentioned in the Introduction (Section 1), PMFs induce gravitational instabilities, scalar (density), vector (vorticity), and tensor (gravitational waves) modes; for more details, see Subramanian (2016) and references therein. In the context of the PMF’s effects on LSS (or vice versa), the scalar mode plays the most important role through modifying the matter power spectrum.¹⁹ The effects on the initial matter power spectrum have been discussed in the pioneering work of Wasserman (1978), Kim et al. (1996), and Gopal & Sethi (2003). All these studies have neglected PMF decay

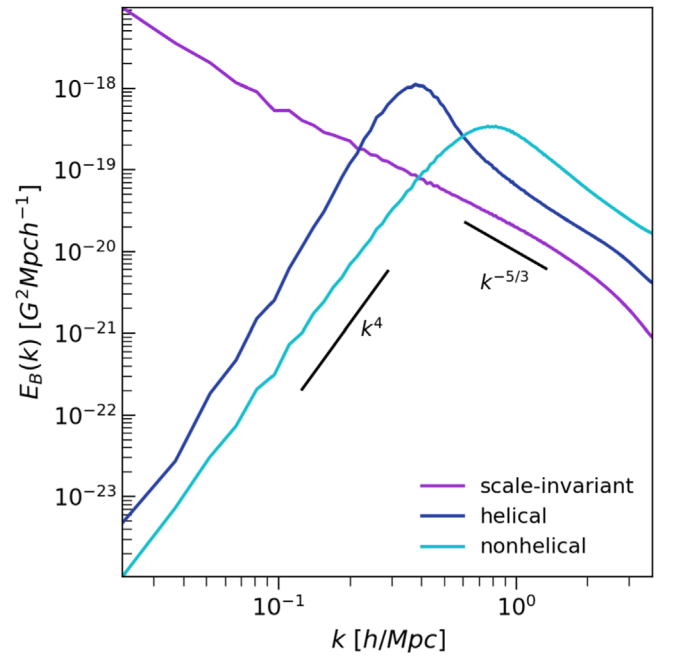


Figure 1. The initial magnetic power spectra for the stochastic setups.

effects, assuming a frozen-in magnetic field with unchanged spectral profile from the moment of generation until recombination. In our work, we consider the MHD decay effects while neglecting the initial matter power spectrum modifications. The self-consistent derivation of the initial linear magnetized perturbation is beyond the scope of this paper. The main novelty of our approach lies in the fact that we adopt a magnetic field from a self-consistent turbulence simulation where the field displays an approximately self-similar decay. In particular, the field contains coherent structures over all length scales.

In addition, recent numerical work has shown that such modifications to the initial power spectrum lead to effects mainly at the low end of the halo mass function (see Sanati et al. 2020; Katz et al. 2021). Such effects should not significantly impact the results presented in this work since our initial magnetic conditions are better suited for studying the evolution of magnetic fields on larger scales and higher-mass haloes. Therefore, the proposed initial conditions are suitable for the questions explored in this work.

3. Physical Model

In this section, we discuss the physical motivation for studying the chosen primordial magnetogenesis models and statistical characteristics for these scenarios. The statistical characteristics of each PMF are determined by the generation mechanism. First, in the case of a uniform, homogeneous PMF that is generated during the inflationary stage, the correlation length λ_B is undetermined (well above the horizon scale at the generation moment). Indeed, such a PMF might be described as a monochromatic field at $k = 0$. Such a field has zero helicity, and no spectrum can be associated to it²⁰ (i.e., the realization in Fourier space is a Dirac delta

¹⁷ We note that we call this model “scale-invariant” even though it has a turbulent spectra with $k^{-5/3}$ scaling; see Section 3.

¹⁸ See, however, Bera et al. (2020), who claim a faster decay of PMFs than expected by the expansion of the universe.

¹⁹ Here, the effects induced through nonlinear coupling between the modes are neglected. We also do not consider the additional vector mode presence that is absent in the standard cosmological scenario, and can change the initial velocity field.

²⁰ It is important to emphasize that such magnetic fields are qualitatively different from the small-scale fields that are obtained by tangling of a uniform (imposed) one. This is because, in periodic domains, such a field constitutes a separate component that can never change. This has dramatic consequences for the evolution of the magnetic field on all smaller scales; see Brandenburg et al. (2020) for examples.

function). If a statistically homogeneous field has been generated through some mechanism after inflation, its peak scale λ_{peak} and therefore its correlation length must be limited by the size of the Hubble horizon at the moment of generation, H_*^{-1} . In this case, we can still use a monochromatic field at a nonzero wavenumber k_{peak} . Correspondingly, the PMF in Fourier space will be approximated by a Dirac delta function as $\delta(k - k_{\text{peak}})$. This is a common description when referring to the lower limits of the magnetic field through blazar spectra observations (Taylor et al. 2011). The energy density associated with a homogeneous PMF is simply given through $B^2/(8\pi)$, regardless of whether the field has finite or infinite correlation length. Therefore, the initial conditions (i) and (ii) (see Section 2.1) represent inflationary-generated fields with unlimited and limited correlation lengths, respectively. In the latter case, we take into account the development of a turbulent forward cascade in the radiation-dominated epoch (Kahniashvili et al. 2017). That is, the inflation-generated, scale-invariant k^{-1} spectra result in a Kolmogorov $k^{-5/3}$ spectrum by the end of recombination.

In the case of causally generated magnetic fields after inflation, the correlation length is limited by H_*^{-1} . Under the standard description of a PMF generated during the electroweak phase transitions through bubble collisions, the physical correlation length is determined by the bubble length scale. A length scale of around one-hundredth of the Hubble horizon scale is commonly assumed, with 100 bubbles within a linear Hubble scale. For the QCD phase transitions, the bubble size is commonly assumed to be one-sixth of the Hubble scale (see, e.g., Schwarz 2003). It is important to realize that the resulting decaying turbulence is invariant under rescaling with the correlation length λ_B such that the magnetic and kinetic energy spectra obey

$$E(k, t) = \lambda_B(t)^{-\beta} \phi(k\lambda_B(t)), \quad (1)$$

where $\beta=1$ for nonhelical MHD turbulence and $\beta=0$ for helical MHD turbulence (Brandenburg & Kahniashvili 2017). This allows us then to rescale our initial magnetic field to any desired epoch based on the value of λ_B . Therefore, at the level of the models discussed in the present paper, there is no difference between turbulence originating from the QCD or the electroweak phase transition.

The cases (iii) and (iv) correspond to a turbulent, causally generated magnetic field with a characteristic scale of $\sim 2.6 h^{-1}$ Mpc and $\sim 1.26 h^{-1}$ Mpc, respectively. Toward larger scales, the magnetic energy spectrum is proportional to k^4 , where k is the wavenumber. This spectrum is referred to as the Batchelor spectrum and occurs for causal PMF generation (Durrer & Caprini 2003). On smaller scales, a turbulent magnetic cascade with an energy spectrum proportional to $k^{-5/3}$ is expected. These spectra are obtained quite generically also when turbulence is driven monochromatically at one wavenumber (Kahniashvili et al. 2021). Physically significant turbulence could be generated during phase transitions through bubble collisions (see Subramanian 2016 and Vachaspati 2021 for reviews) or through the coupling of the inflaton with the magnetic field, possibly shortly after inflation.

Following the results from Brandenburg et al. (2017), the MHD turbulent decay of phase-transitional fields in the radiation-dominated epoch leads to an increase of the magnetic correlation length as a function of conformal time η . If the initial magnetic field is nonhelical, the increase is $\lambda_B \propto \eta^{1/2}$,

whereas if it is fully helical, the increase is $\lambda_B \propto \eta^{2/3}$. This increase is expected from the moment of generation until recombination. If a magnetic field is generated at the horizon scale with a strength limited by BBN, the authors estimate that a fully helical (nonhelical) field may reach a (comoving) magnetic field strength of 0.3 nG (3×10^{-3} nG) at a scale of 30 kpc (0.3 kpc) at the epoch of recombination (see Figure 11 in Brandenburg et al. 2017). The freely decaying turbulence regime is terminated as the baryonic fluid becomes neutral after recombination; then the comoving amplitude, spectral shape, and helicity of the magnetic field stay unchanged until reionization ($z \lesssim 15$).

Our selected initial characteristic scales for models (iii) and (iv) are larger than the mentioned predictions due to our limited resolution of $132 h^{-1}$ kpc. It is therefore important to stress that our initial stochastic, helical, and nonhelical spectra are intended only to emulate the shape that is expected theoretically. In the helical case, we selected a correlation length that is larger than the one in the nonhelical scenario since this is also expected from theory as a consequence of the inverse cascade that helical fields undergo in the radiation-dominated epoch (see Subramanian 2016).

4. Results

4.1. Magnetic Field Strength

We start our analysis by studying the effects of the initial magnetic field strength on the final distribution of magnetic fields in different cosmic environments. In this section, we discuss the results from three different initial magnetic strengths: 0.1 nG, 0.5 nG, and 1 nG (see Table 1).

In Figure 2, we show the median of the magnetic field and temperature distributions with respect to the gas density distribution for the different models at $z=0.02$. In the same figure we also show a 2D histogram, i.e., we overplot the gas mass (for the helical case) falling into each bin. The distributions differ according to the different regions of the cosmic web, i.e., voids, filaments, bridges (the latter two indicated with the shaded region), and clusters. It should be noted that the term ‘‘bridge’’ has recently been applied to regions connecting two merging clusters. We identified bridges in our simulations by visual inspection. The typical range of the overdensity in this environment is given in Figure 2. Notably, we define bridges in a way so that they also include the outskirts of galaxy clusters. It is important to distinguish this environment from large-scale filaments, because currently bridges are the most promising way to observationally detect large-scale warm-hot gas filaments (e.g., Govoni et al. 2019; Reiprich et al. 2021).

The resulting differences between magnetic seedings in each cosmic environment observed in Figure 2 can be summarized as follows:

1. *Clusters.* As we can see from the top panel of Figure 2, the variation of the initial magnetic field strength does not affect the normalized²¹ magnetic field distributions in galaxy clusters; although each model leads to higher final mean values for the higher initial magnetic field realization (see Table 2). The highest median values are observed from the inflationary seedings where the

²¹ Normalized by the corresponding mean field value of the model; see Table 2.

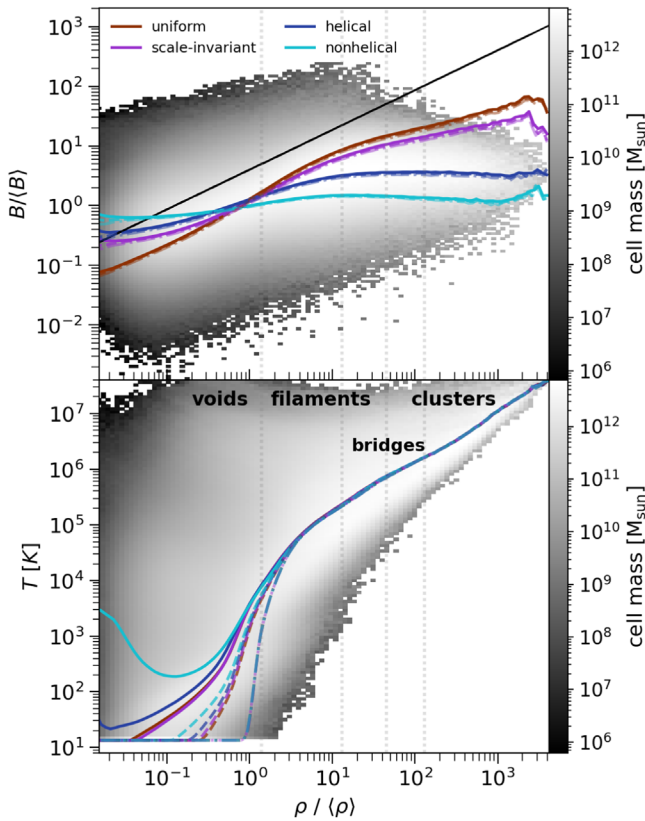


Figure 2. Dependence of the median magnetic field and temperature on density for all of our simulations. The x -axis shows the gas density normalized by the mean density field. The solid, dashed, and dashed-dotted lines correspond to the 1 nG, 0.5 nG, and 0.1 nG normalizations, respectively. The black solid line shows the expected density scaling of the magnetic field strength based on the adiabatic contraction only ($\propto \rho^{2/3}$). The additional color coding (black-white palette) shows the mass of gas (for the helical case) falling into each bin. Vertical dotted lines indicate the characteristic densities in filaments and bridges.

uniform seeding shows a magnetic field strength twice as large as the scale-invariant model. On the other hand, the phase-transitional seedings show the lowest magnetic field strengths within these regions. In particular, the nonhelical case is the model that shows the lowest amplification in galaxy clusters. Interestingly, different seed magnetic fields, as well as the variation of the seed field strength, do not alter the temperature distribution in these regions (see Vazza et al. 2021, for comparison).

2. *Bridges.* Similarly to clusters, the highest magnetic fields in these regions are seeded by the inflationary scenarios. However, the differences in the magnitude of the uniform and scale-invariant cases are reduced in comparison to cluster regions, while for phase-transitional models they are slightly enlarged. Finally, the temperature distribution is again unaffected by different primordial scenarios.
3. *Filaments.* The different initial magnetic field strengths do not alter the normalized magnetic field or temperature trends in this region. However, the final distribution of the magnetic field is affected by the initial topology of the seed field. The seed fields with initial larger characteristic scales lead to larger magnetization levels in filaments. The uniform and scale-invariant cases show amplification due to adiabatic contraction. In the helical and nonhelical

Table 2
Mean of the Magnetic Field Strength at $z = 0.02$ Achieved for all our Models
(See Also Table 1)

Model	Normalization (nG)	$\langle B \rangle_{z=0.02}$ (nG)
Uniform	0.1	0.15
	0.5	0.69
	1	1.29
Scale-invariant	0.1	0.15
	0.5	0.69
	1	1.27
Helical	0.1	0.09
	0.5	0.42
	1	0.79
Nonhelical	0.1	0.08
	0.5	0.39
	1	0.74

Note. Note that the mean value is computed in the whole cosmological box.

models, where the magnetic power of the large-scale modes is smaller (see Figure 1), the amplification due to adiabatic compression is less efficient. Previous work that focused on filaments (e.g., Vazza et al. 2014) have argued that the magnetic amplification within these regions is less dependent on resolution and possible dynamo action even at high Reynolds numbers. This can happen because compressive modes are expected to be dominant in filaments and suppress small-scale twisting of magnetic structures. It remains interesting for future work to assess whether our helical and nonhelical models at higher resolution and, therefore, higher Reynolds number could further amplify magnetic fields by promoting more solenoidal modes within filaments. Finally, it seems that the differences between the inflationary and phase-transitional models are not reflected in the temperature distribution. Similar trends have been found in Gheller & Vazza (2019), where the different seeding scenarios show significant imprints on final magnetic field distributions but only mild differences in the temperature trends (pronounced mostly at high densities).

4. *Voids.* These regions are assumed to be most promising for discriminating among different magnetogenesis scenarios (see, e.g., Dubois & Teyssier 2008; Donnert et al. 2009). We see that differences between the models in the temperature profiles are revealed only for the higher initial magnetic field realizations (i.e., only for the 0.5 nG and 1 nG initial magnetic field strengths). However, the differences between the uniform and scale-invariant models are negligible, while the helical and nonhelical cases show the largest discrepancies. In addition, we see that stochastic (scale-invariant, helical, or nonhelical) seedings lead to the highest magnetic field strengths, and consequently highest temperatures within these regions. This highlights the fact that initial stochastic turbulent motions could cause local heating. Similar trends were obtained by Vazza et al. (2021) where only models with an initial power-law magnetic spectrum were considered. Therefore, initial magnetic

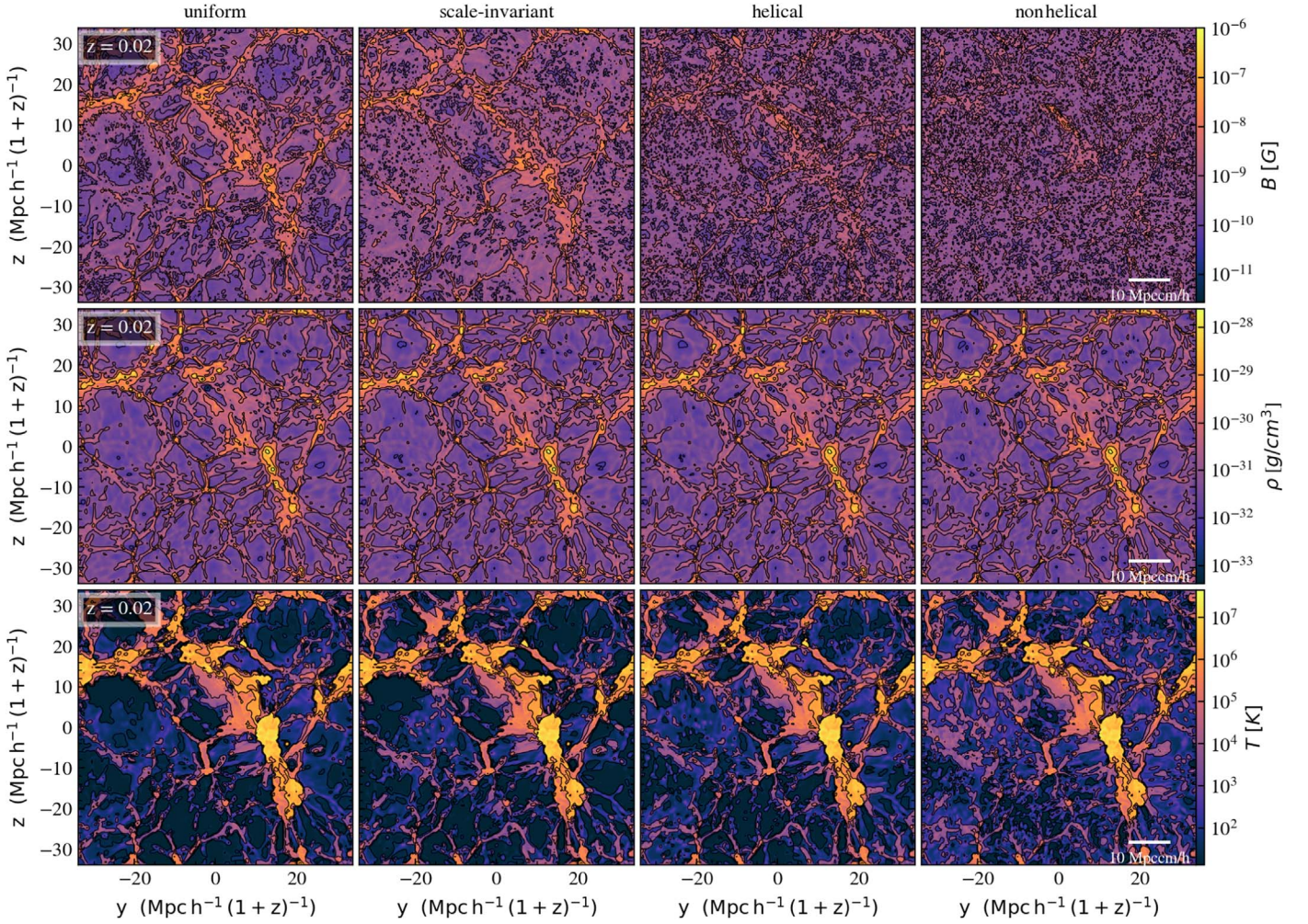


Figure 3. Contoured slices through the center of the simulated box at $z = 0.02$. The top, middle, and bottom panels show the magnetic field, density, and temperature slices, correspondingly. The overplotted contour lines mark the regions with a certain field strength, and the range of the field values are set according to the minimum and maximum of the annotated fields.

fluctuations could be important for the local heating dynamics. In particular, PMFs can heat up the hydrogen and helium in the IGM by, for example, decaying turbulence (see, e.g., Sethi & Subramanian 2005; Minoda et al. 2017) and this can be reflected in the HI 21 cm signal (Sethi 2005; Minoda et al. 2019; Natwariya 2021). Strong absorption spectra of the global HI signal detected by the EDGES experiment suggest that the IGM was colder than expected from the standard cosmological scenario (Bowman et al. 2018). In the recent work of Bera et al. (2020) it has been shown that heating of the IGM due to PMFs along with DM–baryon interactions (Barkana 2018) can be used for constraining the strength of PMFs. Hence, the observed temperature differences in Figure 2 could be used to probe the strengths of both inflationary as well as phase-transitional models in cosmic voids.

We can conclude that the amplification of the initial magnetic field due to adiabatic contraction is subdominant in the stochastic turbulent cases at our resolution. Conversely, the uniform model can be well fitted by the simple $\rho^{2/3}$ relation (expected from adiabatic contraction only) in the filaments and low-density regions (see also Appendix B). As expected, the differences between models become larger at the galaxy-cluster

scales due to our limited resolution. While we expect that these differences should persist (although to a lesser degree) with higher resolution, only future work focusing on these regions can demonstrate it.

For the remaining part of the paper we will focus on the PMF scenarios with an initial 1 nG normalization (see Table 1). The resulting mean magnetic field strengths from this normalization are more in agreement with current observations; see, e.g., Fusco-Femiano et al. (2001, 2004) for the 0.1–1 μG magnetic field strengths found in galaxy clusters based on the inverse Compton measurements from radio haloes, and Vogt & Enßlin (2005) for the strengths as high as 1–7 μG based on the likelihood analysis of Faraday rotation measures.

4.2. General Properties

We show slices of the final ($z = 0.02$) magnetic field, density, and temperature in the $67.7 h^{-1} \text{Mpc}$ box in Figure 3. As we can observe in the top panels of Figure 3, the stochastic seeding fills the voids more efficiently than the uniform case, while the uniform and scale-invariant magnetic seedings show the largest spatial correlation with the filamentary structures. This is not surprising because the initial magnetic power spectrum of the uniform seeding does not have a characteristic scale, and the characteristic scale of the scale-invariant

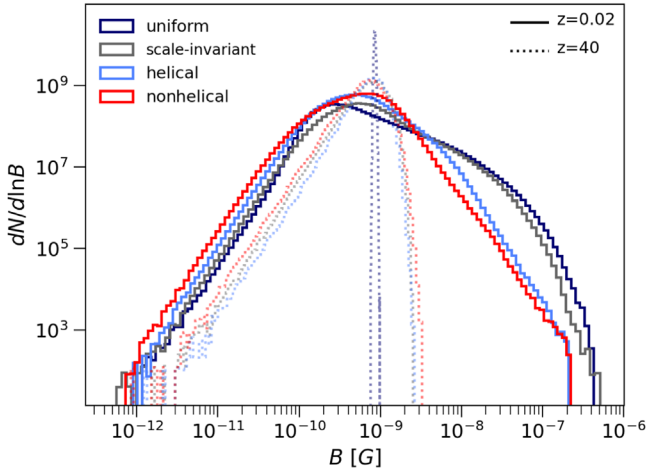


Figure 4. Probability distribution functions for the different magnetic seedings at $z = 40$ (dotted lines) and $z = 0.02$ (solid lines).

spectrum is larger than that of the helical and nonhelical cases. We also observe that nonhelical initial magnetic fields tend to create more substructures than helical ones. This is an expected trend in MHD simulations of helically and nonhelically driven turbulence because of the magnetic helicity (and thereby magnetic energy) transfer to large scales. In a recent study of turbulent dynamos driven by isotropic forcing in isothermal MHD (Väisälä et al. 2021), helical and nonhelical cases were compared. The authors found that an initially Gaussian magnetic field (with a magnetic energy spectrum $\propto k^2$) develops a magnetic energy spectrum with a characteristic scale (peak spectrum) in both cases. Nonetheless, the helical case attains a large-scale nature (more power at k smaller than the peak scale), while the nonhelical case is still characterized by a small-scale structure.

The density (middle row in Figure 3) and temperature (bottom row in Figure 3) contours show a spatial correspondence between the densest structures ($\sim 10^{-28} \text{ g cm}^{-3}$) and the highest temperatures ($\sim 10^7 \text{ K}$) in all four cases. The low-density regions ($\sim 10^{-32} - 10^{-31} \text{ g cm}^{-3}$) enclose higher temperatures in the nonhelical case than in all the other cases. This is a direct consequence of having smaller magnetic substructures in the nonhelical model at the initial and final redshifts, which leads to extra turbulent dissipation in the void regions.

In Figure 4 we show the volumetric probability distribution functions (PDFs) of the magnetic field for all our models. The PDFs are shown for two epochs: $z = 40$ (dotted lines) and $z = 0.02$ (solid lines). The final PDFs show a broadening in all the models. The low-end tail of the distribution (values below $6 \times 10^{-10} \text{ G}$) is very similar for all the models. By contrast, the high-end tail of the distribution (values above $4 \times 10^{-9} \text{ G}$) differs in the inflationary and phase-transitional models. Both inflationary models produce higher magnetic field values than the phase-transitional models. It should also be noted that the PDFs for both scenarios deviate from the Gaussian trend (more evidently seen for the inflationary models) and the peak of the distribution in the inflationary case is shifted toward lower values. For example, in the uniform case, the peak is shifted from $8 \times 10^{-10} \text{ G}$ to $2 \times 10^{-10} \text{ G}$. We can see that the main differences in the distributions come from the regions where the magnetic field strength is of the order of $4 \times 10^{-9} - 5 \times 10^{-7} \text{ G}$.

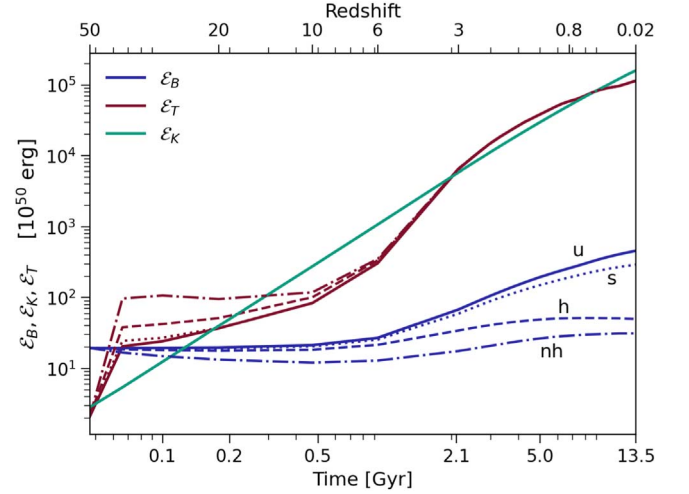


Figure 5. Evolution of magnetic, thermal, and kinetic energies for the different magnetic seedings. The solid, dotted, dashed, and dashed-dotted lines correspond to uniform, scale-invariant, helical, and nonhelical cases, respectively.

Finally, the evolution of thermal, kinetic, and magnetic energies over a time span of 13.5 Gyr is shown in Figure 5. The thermal \mathcal{E}_T , kinetic \mathcal{E}_K , and magnetic \mathcal{E}_B energies are defined as

$$\int nk_B T dV, \quad \int \frac{\rho v^2}{2} dV, \quad \int \frac{\mathbf{B}^2}{8\pi} dV, \quad (2)$$

where n is the gas number density, \mathbf{v} the velocity, k_B the Boltzmann constant, and V the volume. The growth of kinetic and thermal energies achieved in all four models is of the order of $\sim 10^5$ by the end of the simulation. The thermal energies show variations between the models at earlier redshifts (see $z \gtrsim 6$, where stochastic phase-transitional cases show larger thermal energies). This indicates that more dissipative processes are present in these scenarios. Although we find that the extra heating shown in Figure 5 is independent of the Riemann solver, we cannot rule out a numerical origin. However, we also see that the thermal-energy evolution converges to the hydrodynamic case for redshifts $z \lesssim 6$ (see also Appendix C). For this reason, it is unlikely that our analysis at lower redshifts is affected by the initial transient. Moreover, spurious heating will be suppressed by radiative cooling in a more advanced model.

The final thermal and kinetic energies (for $z \gtrsim 6$) show no difference between the four models. However, differences in the magnetic energies arise at a redshift as early as $z \sim 40$. At $z = 0.02$ it is evident that the magnetic energy in the inflationary models is roughly one order of magnitude larger than the magnetic energy in the phase-transitional models. Overall, the magnetic energy growth throughout the evolution is observed to be by a factor of ~ 10 in the uniform and scale-invariant cases, and by a factor of $\sim 2-4$ in the nonhelical and helical cases, respectively.

4.3. Evolution of Magnetic Power Spectra

In this section, we focus on the properties of the magnetic power spectra for the different primordial magnetic seedings. We define the magnetic energy power spectrum in Fourier

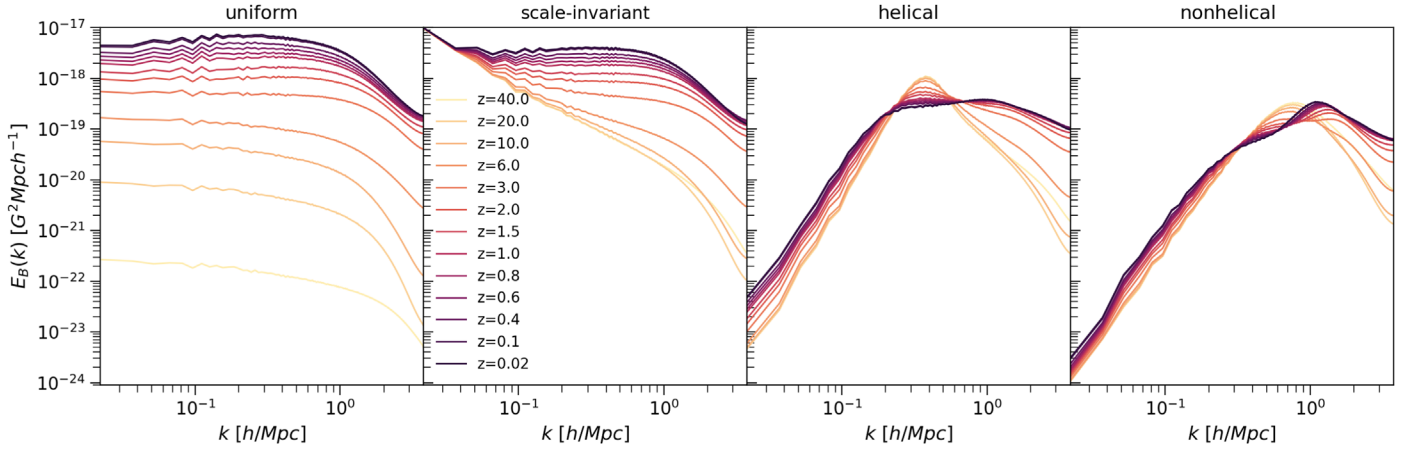


Figure 6. Redshift evolution of magnetic power spectra. From left to right: the uniform, scale-invariant, helical, and nonhelical seedings.

space as

$$\int E_B(k) dk = \frac{1}{2V} \int \hat{\mathbf{B}} \cdot \hat{\mathbf{B}}^* 4\pi k^2 dk, \quad (3)$$

where $\hat{\mathbf{B}}$ denotes the Fourier transform of the magnetic field, $\hat{\mathbf{B}}^*$ is its complex conjugate, $k = |\mathbf{k}|$ is the norm of the wavevector, and V is the volume that normalizes the spectrum.

In Figure 6 we show the evolution of the magnetic power spectra of the inflationary (uniform and scale-invariant) and phase-transitional (helical and nonhelical) cases. Notable features of this figure are as follows:

1. *Inflationary seeding.* The magnetic power spectrum in the uniform and scale-invariant cases reaches higher values at the final redshift than that of the cases with helical and nonhelical seeding. In particular, the uniform seeding shows how the magnetic energy builds up at all scales in a similar fashion from early redshift ($z = 40$). This emphasizes how the magnetic field follows the growth of the density perturbations. On the other hand, the amplitude of the power spectrum in the scale-invariant case starts increasing only from $z = 10$, but the final distribution achieved in this case is similar to that in the case of the uniform seeding.

The obtained trends for these two subcases of an inflationary scenario seem to be different from the results of a recent study by Brandenburg et al. (2020), where the MHD evolution with imposed and scale-invariant initial fields has been compared in the radiation-dominated epoch. They showed that even if small-scale turbulent forcing is applied, the uniform (imposed) field always decays faster than the field with the scale-invariant spectrum. Subsequent studies revealed that the apparent difference between the two types of simulations is caused by the fact that in the present cosmological simulations there is always a large-scale velocity field, which was not the case in the simulations of Brandenburg et al. (2020). However, repeating their simulations with a large-scale velocity field characterized by an initial k^{-2} spectrum produces a rapid growth of the magnetic field also on large scales; see Appendix D, where we demonstrate the tangling of a homogeneous magnetic field by an initial turbulent velocity field with a k^{-2} spectrum. Thus, there is no conflict between these two types of simulations if comparable initial velocity fields are used in both cases.

2. *Phase-transitional seeding.* The initial characteristic scale λ_{peak} in these cases makes the magnetic power spectra evolve in a very different way. Overall, the total amplitude is smaller than in the inflationary cases, as can be observed in Figure 6. Nevertheless, the most interesting result is how the characteristic scale defines the evolution at large and small scales. On large scales ($k \lesssim 1 h \text{ Mpc}^{-1}$), the magnetic field growth is moderate. The helical seeding shows stronger magnetic growth than the nonhelical seeding. This happens because in the former case the initial magnetic perturbations are correlated on larger scales (see Figure 1). It is also possible that helicity leads to larger power on these scales. This is an expected trend in MHD simulations of decaying turbulence where the larger growth is observed for large length scales due to the inverse transfer from small to larger scales; see, e.g., Banerjee & Jedamzik (2004) and Brandenburg et al. (2015). On the other hand, scales smaller than the characteristic scale, i.e., $k \gtrsim 0.4 h \text{ Mpc}^{-1}$ for the helical case and $k \gtrsim 0.9 h \text{ Mpc}^{-1}$ for the nonhelical case, respectively, can grow and reach magnetic levels comparable to the inflationary cases. Additionally, we observe that there is a shift of the peak spectra toward smaller scales (at $z \sim 5$) in both cases as more substructure is building up on galaxy-cluster scales ($\sim 1 \text{ Mpc}$).²² Finally, we also observe magnetic power decay on the peak scales and on the smallest scales at early redshifts ($z > 10$) in both the helical and nonhelical cases. In these cases, most of the magnetic energy is initially contained toward small scales while the matter (and density) power spectrum has most of its power contained on larger scales. This limits, for example, the magnetic energy growth in the two cases at early redshifts (see also the discussion at the end of this section).

We compare the initial and final magnetic power spectra with the corresponding linear mass scales for all the models in Figure 7. Note that these mass scales should not be interpreted as the masses of the massive objects (e.g., galaxy clusters) since they can only be accepted as an estimation of masses at certain radii that are still in the linear regime (i.e., these would be the largest scales in our simulations, $k \lesssim 0.5 h \text{ Mpc}^{-1}$). The

²² It should be noted that after the first shift of the peak, the peak again gradually moves from smaller to larger scales (from $z = 3$); this behavior is similar to the aforementioned inverse cascade. This trend is more evident for the nonhelical case.

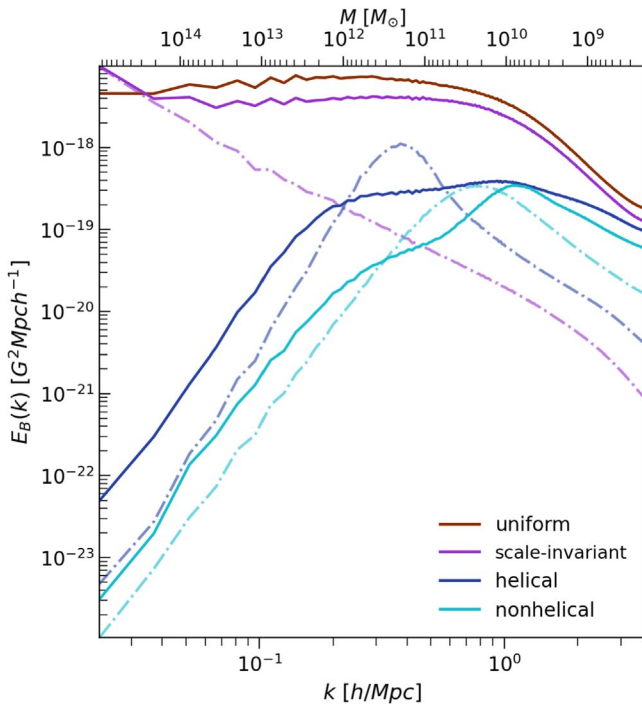


Figure 7. Magnetic power spectra for the uniform and stochastic cases. The dashed-dotted lines show the corresponding power spectra at the initial redshift ($z = 50$) and the solid lines at the final, $z = 0$ redshift.

difference between the amplitudes of the inflationary and phase-transitional magnetic power spectra is more evident at small wavenumbers. As we mentioned above, in Figure 7 the spectra peak of the two stochastic seedings are shifted toward larger wavenumbers. In addition, we see that different phase-transitional seedings are expected to be harder to distinguish at masses $M \lesssim 10^{10} M_\odot$, whereas the magnetization at masses $M \gtrsim 10^{12} M_\odot$ is distinguishable for the inflationary and phase-transitional models. The reader may note that the behavior of the magnetic amplification at different scales is strongly affected by the spectrum peak (or by the coherence scale) at the initial redshift. The role of the peak position will be considered in future work.

The differences between the uniform and scale-invariant spectra for all mass scales is remarkably small. It is only at $3 \times 10^{14} M_\odot$ that the amplitude of the scale-invariant spectra is higher than that of the uniform model. Overall, we discern these differences in the amplitude of the power spectrum between the inflationary and phase-transition models to be increased on larger scales ($M \gtrsim 2 \times 10^{10} M_\odot$) reaching an order of 10^5 difference on mass scales $\gtrsim 10^{14} M_\odot$.

In a collapsing magnetized region, field amplification mainly occurs via adiabatic contraction. However, if that region contains a randomly oriented magnetic field, there are two additional things to consider: (1) the cancellation of opposite-polarity fields can reduce the magnetic flux, and/or (2) there could be extra field amplification by turbulent dynamo if the growth rate is faster than the gravitational compression rate (see also Seta et al. 2018; Seta & Federrath 2020). In our study, shocks that originate during structure formation can additionally affect the magnetic amplification since they can destroy coherent small-scale structures. This can also contribute to decreasing power of the peak scales of helical and nonhelical cases at early redshifts. All these effects explain why in the

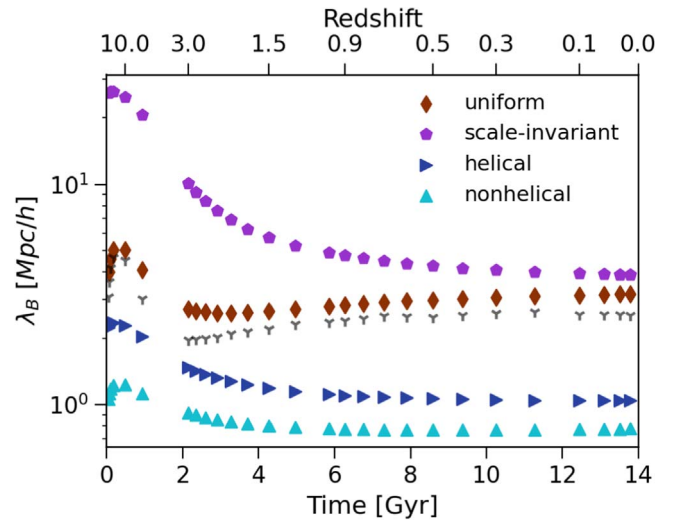


Figure 8. Evolution of magnetic correlation length obtained from different magnetic seedings. Gray points show the correlation length computed from the density power spectrum.

helical and nonhelical cases we see less efficient amplification on both small and large scales (see Figure 6). While all our four cases are affected by the not-well-resolved turbulent motions within the collapsing regions of the cosmic web, the lower magnetic power increase observed in the two phase-transitional cases could be partly attributed to field cancellation (see also discussion below on the correlation length). On the other hand, the stochastic, scale-invariant case develops a nonzero mean field (due to an initial larger correlation length in this case) which makes its evolution very similar to that of the uniform case and less subject to field-cancellation effects. Hence, we observe a larger magnetic field amplification in this case.

Finally, we show in Figure 8 the evolution of the magnetic correlation length, defined as

$$\lambda_B = \frac{\int_0^\infty dk k^{-1} E_B(k, t)}{\int_0^\infty dk E_B(k, t)}. \quad (4)$$

It should also be emphasized that for inflationary, uniform magnetic fields, the correlation length at the initial redshift can be ill-defined, because the numerator of Equation (4) diverges for $k \rightarrow 0$, so this point needs to be excluded. For our nearly scale-invariant field, however, the spectral energy goes to zero for $k \rightarrow 0$, and thus the integral does not diverge; see Brandenburg et al. (2018) for details.

In all four models, we see an increasing trend at initial redshifts which mostly follows the evolution of the density correlation length. In unigrid Eulerian cosmological simulations, the density power spectrum tends to be more damped at small scales since the gravity forces are smoothed at the grid scale, as noted by Hahn & Abel (2011). This slower growth of the smallest scales leads to the increase of the magnetic and density correlation length at $z > 10$ in Figure 8.

The correlation-length evolution is followed by a decrease ($z \lesssim 10$) in both density and magnetic correlation lengths for all four models. This results from the small-scale modes entering the nonlinear regime of the growth of density perturbations. At this stage, power is transferred from large to small scales. A final increase of magnetic correlation length is only noticeable in the uniform seeding case at $z \lesssim 1.75$. The trends in the redshift range 1.75–0 follow $t^{0.16}$, $t^{-0.34}$, $t^{-0.11}$, and $t^{-0.03}$ for

the uniform, scale-invariant, helical, and nonhelical cases, respectively. The density correlation length shows a similar trend as the magnetic correlation length in the uniform case, although with a slower increase with $l^{0.13}$. It should be noted that the latter trend could also be affected by the damped growth of perturbations at small scales because of our limited resolution.

Finally, we see that the correlation length in the uniform case is about twice as large as in the helical and nonhelical cases, and the scale-invariant model shows the largest final correlation length ($\sim 4 h^{-1}$ Mpc). This is in line with our previous discussion on the discrepancies in magnetic amplification of inflationary and phase-transitional cases.

4.4. Faraday Rotation Measures

Faraday rotation of linearly polarized sources is a powerful observational approach that can help us understand magnetic fields on a vast range of astrophysical scales. Polarized radio emission from distant sources is affected by an intervening magnetized plasma which rotates the intrinsic polarization plane. The differential angle of rotation is proportional to the square of the emitted wavelength λ^2 and to the rotation measure (RM). For a source at cosmological distance and redshift z , RM is defined as

$$\begin{aligned} \text{RM} &= \frac{e^3}{2\pi m_e^2 c^4} \int_0^{l_s} (1+z)^{-2} n_e(z) B_{\parallel}(z) dl(z) \\ &= 0.812 \int_0^{l_s} (1+z)^{-2} \left(\frac{n_e}{\text{cm}^{-3}} \right) \left(\frac{B_{\parallel}}{\mu\text{G}} \right) \left(\frac{dl}{\text{pc}} \right) \frac{\text{rad}}{\text{m}^2}, \quad (5) \end{aligned}$$

where e , m_e , and c are the electron charge, electron mass, and speed of light, respectively; n_e is the electron number density, B_{\parallel} is the magnetic field component along the line of sight (LOS), and dl is the integration path length. In this section, we use physical quantities, such as physical magnetic field strength, electron number density, and physical length scales. A positive (negative) RM implies a magnetic field pointing toward (away from) the observer. Note that, in general, Equation (5) defines the Faraday depth ϕ , which is inferred from observations through the method of RM synthesis (Burn 1966; de Bruyn & Brentjens 2005). The RM coincides with Faraday depth in the ideal case when the rotation is caused by only one, nonemitting Faraday screen.

RM observations of extragalactic radio sources are fundamental in further constraining the properties of large-scale magnetic fields in the near future. In particular, they will be of greatest importance for discriminating between magnetogenesis scenarios because of their possibility to constrain the magnetization in the still poorly constrained regions of the cosmic web, i.e., filaments and voids. As the extragalactic polarized emission travels through the magnetized medium between source and observer, there are various contributions along the LOS that add up to the total observed RM. One relevant contribution comes from the Milky Way (see Hutschenreuter et al. 2021), but there have been recent efforts in constraining the extragalactic contribution alone (e.g., Schnitzeler 2010; Oppermann et al. 2015; Vernstrom et al. 2019; O’Sullivan et al. 2020). These recent RM observations have constrained the extragalactic RM variance to $5\text{--}10 \text{ rad m}^{-2}$ at 1.4 GHz. At lower frequencies,

O’Sullivan et al. 2020 limit the extragalactic contribution to $< 1.9 \text{ rad m}^{-2}$ (measured at 144 MHz).

In Figure 9 we show the RM maps of the simulated cosmic web at $z=0.02$ for different primordial seeding cases. Note that we did not include the Galactic contribution (Hutschenreuter et al. 2021). These maps have been obtained by integrating Equation (5) along the x -axis. We checked that the selected axis of projection does not produce differences in the results described in this section. We observe significant differences in the RM maps for the different primordial seeding models. First, we observe more coherent structures in the uniform and scale-invariant seeding cases than in the helical and nonhelical cases. Second, the RM values are highest for the inflationary scenarios and lowest in the helical and nonhelical ones. This result is a consequence of the RM being an integrated quantity. The sum of coherent magnetic fields will give rise to a strong RM signal, which is the case in the uniform and scale-invariant models (see first and second panels of Figure 9). On the other hand, the sum of stochastic magnetic fields can cancel out and weaken the RM signal (see third and fourth panels of Figure 9). In addition, the RM maps are determined by the total level of magnetization at this epoch (see Table 2). The helical and nonhelical seedings lead to lower magnetization levels in filaments, as was discussed in Sections 4.2 and 4.3. Therefore, this adds to the discrepancy observed between inflationary and phase-transitional models. We also note that uniform seeding leads to higher Faraday rotation than the scale-invariant seeding. This seems to be in agreement with Vazza et al. (2021), where the authors explored also a uniform seed field and various seeds described by power laws. Nevertheless, our inflationary results cannot be directly compared to this recent work since they applied a subgrid dynamo model for further magnetic amplification.

In Figure 10 we show the corresponding PDFs for the absolute value of RM at $z=0.02$. We additionally show the PDF for the regions excluding galaxy clusters (dotted lines), and for galaxy clusters with the overdensity criterion $\rho/\langle\rho\rangle \geq 1.3 \times 10^2$ (filled histograms). These criteria were applied before computing the integral defined in Equation (5). The distributions accounting for the whole $67.7(h^{-1} \text{ Mpc})^3$ region, as well as distributions excluding galaxy clusters, peak at 1.6×10^{-3} , 4×10^{-3} , 1.2×10^{-2} , and $1.7 \times 10^{-2} \text{ rad m}^{-2}$ for the nonhelical, helical, scale-invariant, and uniform cases, respectively. When considering only the highly ionized regions (clusters; $T > 10^6 \text{ K}$), the PDFs peak at 1.5×10^{-2} , 4.5×10^{-2} , 0.3, and 0.5 rad m^{-2} for the nonhelical, helical, scale-invariant, and uniform cases, respectively. We see that the highest RM values are obtained at these highly ionized regions for the four models. As can also be seen in Figure 9, the highest values of RM tend to follow the collapsed structures. Similar trends have been observed in other cosmological simulations (see, e.g., Marinacci et al. 2015). In line with Figure 9, we find that the highest RM values are observed for the two inflationary models.

In the following, we extend the analysis to a range of redshifts. In Figure 11 we show the redshift evolution of the mean and rms statistics of $|\text{RM}|$ within different environments and for different seeding scenarios. We analyzed a total of 20 cosmological boxes (corresponding to 20 redshift bins) in a redshift range $3 \leq z \leq 0.02$. This range is particularly relevant, for example, for the upcoming WEAVE-LOFAR survey (Smith et al. 2016), where one expects to obtain spectroscopic

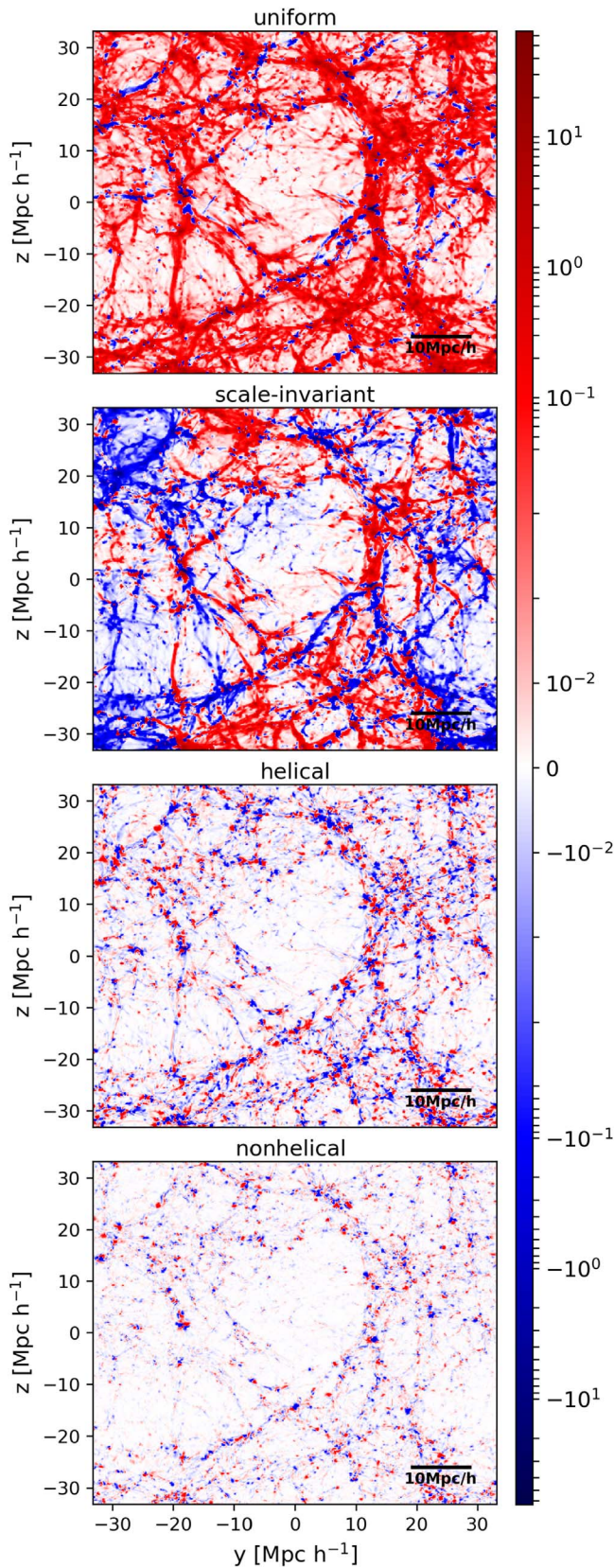


Figure 9. Faraday rotation maps from the simulated cosmic web at $z = 0.02$. From top to bottom: uniform, scale-invariant, helical, and nonhelical cases, respectively. The color bar shows values in $[\text{rad}/m^2]$ and it is linearly scaled in the range $[-0.04, 0, 04]$.

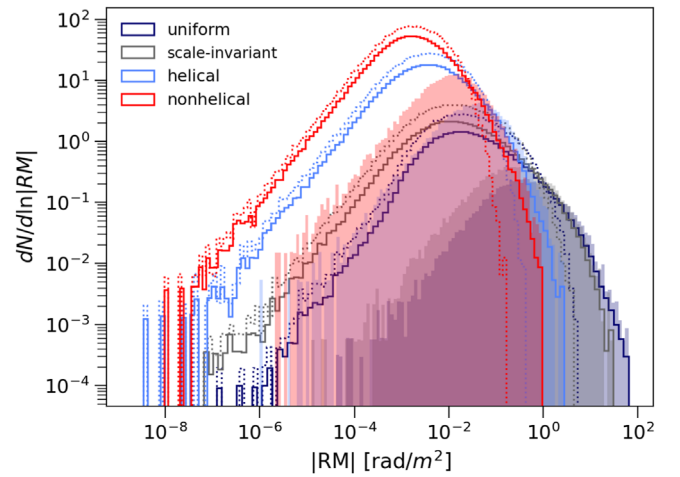


Figure 10. Distribution functions of the absolute RM for different seeding models. The dotted lines show the contribution to the total PDF from the regions excluding galaxy clusters while the filled histograms represent contributions from galaxy clusters ($\rho/\langle\rho\rangle \geq 1.3 \times 10^2$).

redshifts for all polarized radio sources detected in the LOFAR Two-meter Sky Survey (LoTSS; Shimwell et al. 2019) up to $z < 1$. In the first column of Figure 11, we show the statistics from the whole simulating box while the second and third columns show the RM statistics in the regions excluding galaxy clusters and in the warm-hot intergalactic medium (WHIM), respectively. The regions excluding galaxy clusters imply the same criterion as in Figure 10, while for the WHIM region we additionally set the temperature criterion $10^5 \text{ K} \lesssim T \lesssim 10^7 \text{ K}$. Due to cosmological expansion, it is expected that the mean and rms RM will decrease with time. This is in particular true for the lowest-density regions of the cosmic web where there is almost no turbulent amplification (see the second and third columns of Figure 11). As we can see, the highest rms and mean $|\text{RM}|$ values are obtained when including cluster environments and in the WHIM, which are the densest regions. The first is consistent with previous numerical work, where it has been found that the resulting RM is dominantly contributed by the density peaks along the LOS (e.g., Akahori & Ryu 2010, 2011). Note that in these regions our reported RM values are lower than the typical observed values due to our limited resolution (see discussion in Section 5). RMs of hundreds rad m^{-2} have been observed in clusters (see Böhringer et al. 2016, for a sample of galaxy clusters). Since clusters are especially underresolved in our simulations, the RM values in these regions should be interpreted only as lower limits.

We characterize the $|\text{RM}|_{\text{rms}}$ evolution by fitting the data to the following equation: $|\text{RM}|_{\text{rms}} = \text{RM}_0(1+z)^\alpha$. We show the fitted values for each environment for the four models in Table 3. Since the definition of RM (see Equation (5)) includes the proper values of the electron density, magnetic field, and integration path length, we expect it to scale as $\text{RM} \sim (1+z)^2$, with $\alpha = 2$. However, as we can see from Table 3, $\alpha < 2$ for all environments in the uniform and scale-invariant case, i.e., the decrease of RM values with redshift will be slower in these scenarios. This means that magnetic fields along with density

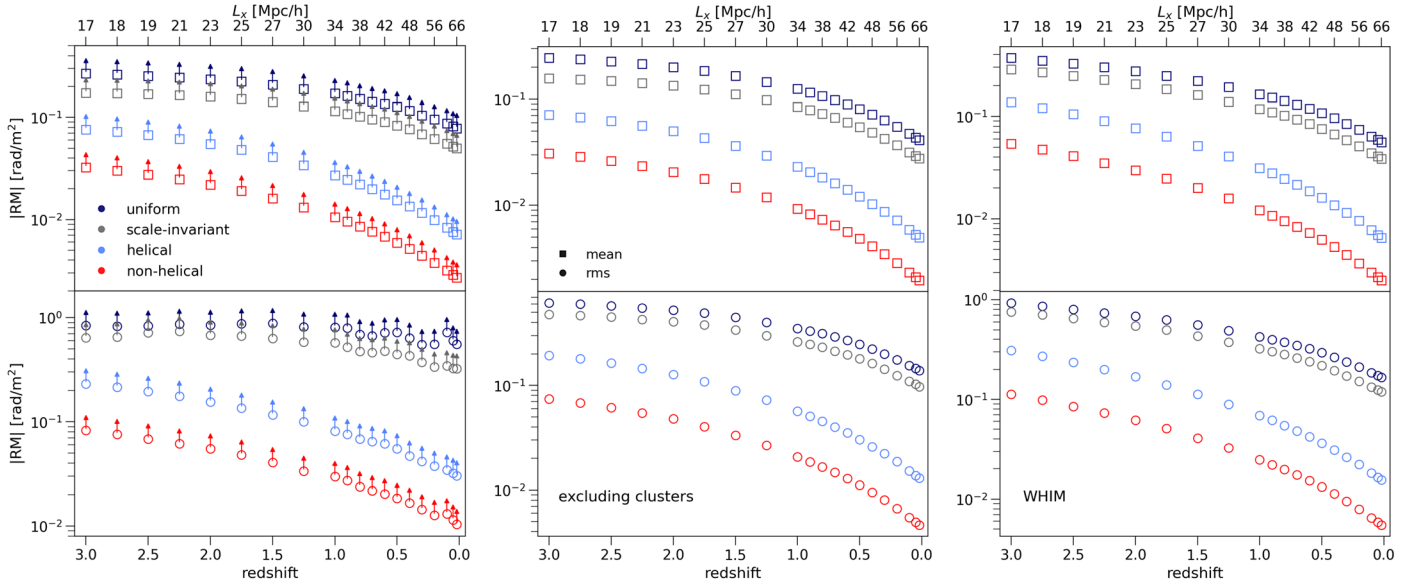


Figure 11. Redshift evolution of the mean and rms statistics of the absolute $|RM|$ for the whole simulating volume (first column), for the regions excluding galaxy clusters ($\rho/\langle\rho\rangle < 1.3 \times 10^2$; second column) and for the regions satisfying the criteria for WHIM ($10^5 \leq T \leq 10^7$, $\rho/\langle\rho\rangle < 1.3 \times 10^2$; third column). The upper panels show the mean values and the lower panels show the rms values. Statistics of all these regions exclude the lowest-density regions (satisfying the $\rho/\langle\rho\rangle < 2 \times 10^{-2}$ criterion).

Table 3
Fitted Values of $|RM|_{\text{rms}} \propto RM_0(1+z)^\alpha$ of Figure 11 for Different Environments of our Simulations

Model	Environment	RM_0	α
Uniform	Exc. clusters	0.15	1.12
	WHIM	0.17	1.26
	All	0.59	0.31
Scale-invariant	Exc. clusters	0.11	1.20
	WHIM	0.12	1.36
	All	0.34	0.61
Helical	Exc. clusters	0.01	2.03
	WHIM	0.02	2.21
	All	0.03	1.15
Nonhelical	Exc. clusters	0.01	2.07
	WHIM	0.01	2.22
	All	0.01	1.52

do not only decrease in these regions, as is expected by the expansion of the universe, but are subject to amplification.

Recently, Vernstrom et al. (2019) and O’Sullivan et al. (2020) presented a new approach in order to isolate the extragalactic RM variance. The method relies on comparing pairs of extragalactic radio sources and computing the RM difference between them. Following O’Sullivan et al. (2020), the statistical results come from comparing the RM from sources at the same redshift (named as physical pairs), e.g., double-lobed radio galaxies, and from sources at different redshifts (named as random pairs). In order for us to analyze our simulations and compare to these recent work, we would have to carry out a careful study of stacking cosmological boxes (see Thomas & Carlberg 1989 and Scaramella et al. 1993, for pioneering work) and defining light cones before integration (see Akahori & Ryu 2011 and Vazza et al. 2021, in the context of RM). Such a study is out of the scope of this

paper and we leave it for future work. Nevertheless, we can give a first-order estimate on the RM difference by using the information in Figure 11. We considered the $|RM|$ distribution function of the simulation box to be representative of each redshift. In this way, we select the variance of the distribution to be the representative value at each redshift.

We analyzed a total of 20 redshift bins up to $z = 3$, where we obtained 190 different combinations of redshift pairs. Note that here we do not take into account the spatial distribution of possible sources within each simulation box. Instead we assume the PDF statistics to be representative of the simulation box at that redshift. We refer the reader to Appendix E for a word on the distribution of sources as a function of redshift.

We compute the variance in the environment where we exclude the regions of galaxy clusters (see second column of Figure 11) and the WHIM environment (see third column of Figure 11). These two environments are less affected by our low resolution. We are also interested in these environments because LOFAR is not expected to detect polarized sources from intervening clusters (e.g., Stuardi et al. 2020). As a second step, we compute the average variance between each selected redshift (random) pair, i.e., taking into account all redshift bins in between the pair. Once this is done for all 190 pairs, we compute the rms of all the variances. This procedure yields an rms upper limit in the WHIM of 0.7, 0.6, 0.3, and 0.2 rad m^{-2} for the uniform, scale-invariant, nonhelical, and helical cases, respectively. The environment where we only exclude galaxy clusters gives similar values: 0.6, 0.5, 0.3, and 0.2 rad m^{-2} , respectively. These RM values are marginally lower than the results reported at 144 MHz in O’Sullivan et al. (2020). After analyzing the difference between physical and random pairs, the authors concluded that the excess Faraday rotation contribution between random pairs has an upper limit of 1.9 rad m^{-2} . This work places an upper limit of 4 nG for a PMF. A similar analysis at 1.4 GHz and in a redshift range $0 < z < 1$ was done in Vernstrom et al. (2019), where the authors obtained an excess contribution between random pairs of

10.3 rad m^{-2} . In this case, the authors placed an upper limit of $\sim 37 \text{ nG}$. Our rms RM values suggest that an initial magnetic seed larger than 1 nG for the four different seedings is required to meet these particular observational RM upper limits. We can give crude estimates of the initial magnetic field strength by asking ourselves which initial magnetic field strength is needed to reach the upper limit of 1.9 rad m^{-2} for all our models: the results of the uniform, spatially homogeneous field (the Mukohyama model) and the scale-invariant, inflationary field would suggest an initial magnetic field strength of $\sim 3 \text{ nG}$. This is comparable to LOFAR results and remains below the upper limits of O’Sullivan et al. (2020) and Vernstrom et al. (2019). Nevertheless, this crude approach alone cannot strictly rule out the $\sim 1 \text{ nG}$ normalization (see discussion below); the phase-transitional models would allow for an even larger initial magnetic seed, namely a magnetic field strength of a primordial stochastic seed (helical or nonhelical) $\sim 6 \text{ nG}$. These values could be in agreement with CMB constraints of helical ($\sim 5.6 \text{ nG}$) and nonhelical ($\sim 4.4 \text{ nG}$) PMFs (e.g., Planck Collaboration et al. 2016). Yet these high values conflict with recent Planck, ACT (Atacama Cosmology Telescope), and SPT (South Pole Telescope) constraints of a $\sim 0.05 \text{ nG}$ PMF (see Galli et al. 2022). It is important to stress that a one-to-one comparison with these recent RM observations is not strictly possible since the reported upper limits are also influenced by environmental selection effects. In this sense, we can only conclude that our first-order approximation RM analysis favors more inflationary PMFs than phase-transitional PMFs. While future simulations with a more sophisticated RM analysis could improve our predictions, future observations that will better isolate the RM signal from the diffuse WHIM and/or voids and filaments will play a decisive role in discriminating PMF models.

We expect great advances with LOFAR in the coming years. There has been significant progress in overcoming challenges in observations by using the ionospheric RM error correction techniques (e.g., Sotomayor-Beltran et al. 2013). These techniques have significantly improved and will be crucial for the accurate calibration of not only the next LOFAR surveys but also for the Square Kilometre Array (SKA). Indeed, the SKA-Low and SKA-Mid (Braun 2015, and references therein) is expected in coming years to provide stronger constraints on the magnetization of the universe. The increased expected number of polarized sources and knowledge of spectroscopic redshifts will enable us to make better comparisons with cosmological simulations. We expect that these advances can further help us to distinguish between the possible origins of cosmic magnetism. The present work shows that scale-invariant and phase-transitional helical and non-helical models still cannot be rejected. In future work, we will study a more extended range of initial conditions in parallel with the stacking technique and definition of light cones to put more stringent constraints.

5. Numerical Aspects

The spatial resolution adopted in the present simulations place limitations on our results. Our resolution is not sufficient to resolve, for example, the additional magnetic amplification within galaxy clusters (Xu et al. 2009; Vazza et al. 2018; Steinwandel et al. 2021). Nevertheless, in Appendix B we show that our results are robust at least on scales $\gtrsim 1 \text{ Mpc } h^{-1}$. We have checked the convergence of the magnetic energy

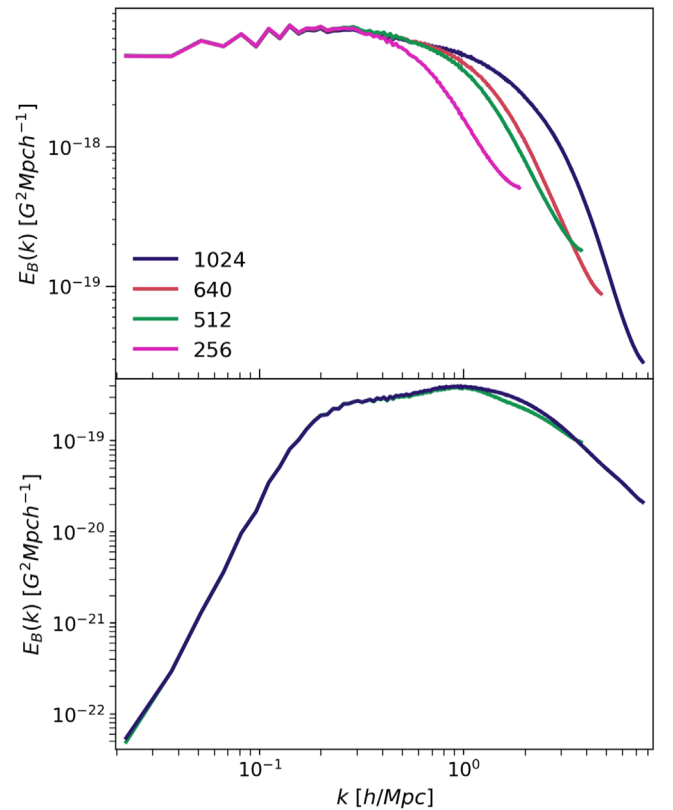


Figure 12. Magnetic energy power spectrum with increasing resolutions (comoving: $264 \text{ h}^{-1} \text{ kpc}$, $132 \text{ h}^{-1} \text{ kpc}$, $105 \text{ h}^{-1} \text{ kpc}$, $66 \text{ h}^{-1} \text{ kpc}$) for the uniform (top panel) and helical cases (bottom panel) at $z = 0.02$.

power spectrum in the whole simulation box with increasing resolution (see Figure 12 in Appendix B). As expected, increasing the resolution results in higher power at higher wavenumbers. On the other hand, we have also checked the trends of the magnetic field compared to the density for the phase-transitional helical and inflationary uniform cases at different resolutions (see Figure 13 in Appendix B and corresponding discussions). In the uniform scenario, there is no substantial change in the overall trends at higher resolution. On the other hand, the phase-transitional helical case shows subtle differences in filaments and voids, while the main differences are observed in the overdensity regions corresponding to galaxy clusters. This seems to indicate that our results on the global properties of the filament and void regions, as well as the differences between the primordial models in those regions, are robust for the present goal of this work. Simulations with adaptive mesh refinement (AMR) are needed to fully assess the discrepancies between primordial seeds within galaxy clusters.

We also tested the dependence of our RM results on the adopted spatial resolution in Appendix B. We show the distribution of RM at $z = 0.02$ at different resolutions for the uniform scenario in Figure 14. At double resolution, the $|\text{RM}|$ values converge for the environment excluding clusters, while for the cluster environments we still see higher (lower) RM values at the high-end (low-end) tail of the distribution. We expect the same follows for the stochastic scenarios.

We used the Dedner cleaning algorithm to impose the $\nabla \cdot \mathbf{B} = 0$ condition (Dedner et al. 2002). The main limitation of this method compared to constrained-transport schemes is

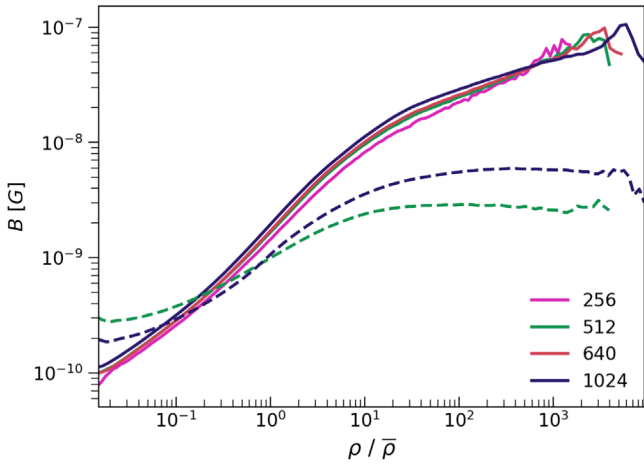


Figure 13. The median magnetic field vs. overdensity profile for increasing grid points (256, 512, 640, 1024) at $z = 0.02$. Solid lines: uniform seeding case; dashed lines: helical case.

the intrinsic dissipation of the scheme by cleaning waves, which reduces the magnetic spectral bandwidth to keep the numerical divergence under control (see Kritsuk et al. 2011). The Dedner formalism has been tested to be robust, accurate, and to converge quickly to the right solution for most idealized test problems (e.g., Wang & Abel 2009; Wang et al. 2010; Bryan et al. 2014) and for other more realistic astrophysical applications (Hopkins & Raives 2016; Tricco et al. 2016; Barnes et al. 2018), as long as the resolution is conveniently increased.

As mentioned in Section 2, we neglected physical processes associated with radiative gas cooling, chemical evolution, stellar and active galactic nuclei feedback. In this way, we can solely focus on the effects of different primordial magnetic seeding through LSS formation. However, these unaccounted for processes are known to pollute the rarefied regions of the cosmic web and, thus, they can potentially lower the possibility of detecting the imprints of different PMFs (see, e.g., Marinacci et al. 2015). We refer the reader to Vazza et al. (2017) for a comparison between the predictions of primordial and astrophysical seeding scenarios of magnetic fields with the `Enzo` code.

In addition, as an important caveat, we note the effect of different Riemann solvers on our results. The most diffusive Riemann solver (local Lax–Friedrichs, LLF; Kurganov & Tadmor 2000) of ENZO affects the evolution of magnetic energy in the tested nonhelical case and decreases it by factor of 2 at final redshifts (see Appendix C for more details). Consequently, the magnetic field and temperature distributions in the void regions also show lower values at $z = 0.02$ for the phase-transitional cases. In the uniform case, on the other hand, we do not observe changes in temperature and magnetic fields due to the LLF solver. We also checked the effect of the DEF used in our simulations, which controls thermal energy in highly supersonic bulk flows. We verified that the DEF does not affect the magnetic field distribution neither in the uniform case nor in the stochastic, nonhelical case. This holds for both Riemann solvers, LLF and HLL. Nevertheless, the DEF affects the temperature distribution, as expected. We caution the reader on the interpretation of the regions where shocks and discontinuities are created by the extreme gravitational forces.

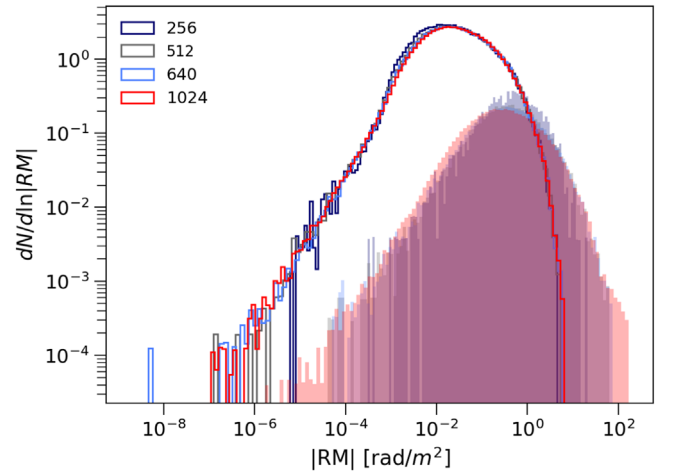


Figure 14. $|RM|$ distribution function dependence on resolution (comoving: $264 h^{-1}$ kpc, $132 h^{-1}$ kpc, $105 h^{-1}$ kpc, $66 h^{-1}$ kpc) at $z = 0.02$ for the uniform seeding. The solid lines represent regions excluding galaxy clusters, while the shaded areas show distributions only for galaxy clusters.

However, we do not expect these regions to be statistically significant to modify the obtained trends from our simulations.

The initial conditions used in the simulations do not account for the effect of magnetized perturbations on the initial matter power spectrum (as in, e.g., Kahnishvili et al. 2013; Sanati et al. 2020, and Katz et al. 2021), which would give us a self-consistent view of the cosmological initial conditions. Nevertheless, it has been recently shown that such effects will only have an impact on smaller haloes and on scales $\sim k > 1 h \text{ Mpc}^{-1}$ (see Katz et al. 2021). Therefore, we would not expect significant changes in our results at the largest and most massive components of the cosmic web.

Finally, in our work we have excluded the nonideal MHD processes, meaning that the viscous and resistive dissipation are not modeled realistically and, therefore, the magnetic Prandtl number, i.e., the ratio of kinematic viscosity and magnetic diffusivity, is effectively unity. This approach is reasonable enough given the existing uncertainties and the difficulties in the characterization of galaxy clusters (see, e.g., Schekochihin et al. 2004; Beresnyak & Miniati 2016) and larger cosmological scales. Furthermore, the ideal MHD description allows us to easily compare our work with previous work (see, e.g., Alves Batista et al. 2017; Marinacci et al. 2018; Vazza et al. 2021). Studying higher Prandtl numbers is out of the scope of this work.

6. Conclusions

In this work we have investigated the evolution of PMFs through the formation of LSS. For the first time, we have compared inflationary and phase-transitional initial seed magnetic fields with cosmological MHD simulations. We have explored four types of initial magnetic seeds: (i) spatially homogeneous (uniform) and (ii) statistically homogeneous (scale-invariant) magnetic fields generated in an inflationary epoch, and (iii) helical and (iv) nonhelical magnetic fields representing a phase-transitional scenario. In the latter three models the initial magnetic spectra reflect the physics of the early universe when the magnetic seed develops Kolmogorov-like turbulent spectra through its MHD decay, while the former case mimics a primordial magnetogenesis according to the Mukohyama model (Mukohyama 2016).

The main results of our work can be summarized as follows:

1. *The role of the initial magnetic field strength.* A higher normalization of the initial magnetic field leads to higher magnetic field values at later redshifts. However, the overall trend of the distribution of final magnetic fields in different cosmic environments is not affected by the amplitude of the initial seed field. Regarding the temperature distribution, we note that phase-transitional seedings (nonhelical case) may lead to extra heating in the void regions as a result of possible turbulent decay of these fields. In addition, the higher (initial ≥ 0.5 nG) magnetic field realization reveals larger differences between the inflationary and phase-transitional models. This suggests that an impact of the stronger initial seed fields will be imprinted on rarefied cosmic regions. Hence, both the strength and topology of the seed fields will be of notable relevance for studies accounting for the effects of magnetic fields on the reionization history of the universe (Sethi & Subramanian 2005; Minoda et al. 2017).
2. *Traces in the cosmic web.* Phase-transitional and inflationary scenarios lead to variations in the final magnetic field distribution of the cosmic web. The magnetic amplification in the inflationary models tends to follow the law of adiabatic gas contraction in voids (partially) and filaments, while a deviation from this law is evident in the phase-transitional models. The overall magnetization of galaxy clusters and bridges as well as of voids in the inflationary models can be orders of magnitude higher than in the phase-transitional scenarios, although the differences between the models on the galaxy clusters' and bridges' scales will be a subject of our future study (and should be confirmed with higher-resolution runs). Discernible differences (with a lower magnitude) between the seeding scenarios are also observed in filamentary structures, where again inflationary seed fields show the largest magnetic amplification.
3. *Possible inverse cascade.* The characteristic peak of the magnetic power spectra in the phase-transitional helical and nonhelical cases shifts toward small scales at late redshifts, $z < 6$. This means that, during this epoch, preferred scales due to structure formation would initially quench the energy transfer from small to large scales. At later stages, $z < 3$, we observe a shift of the peak spectrum from small to large scales in the nonhelical case without an increase of correlation length, though. Therefore, our results cannot unambiguously confirm the existence of an inverse cascade.
4. *Magnetic correlation length.* The final correlation length in the inflationary seedings is larger than that in the phase-transitional seedings (reaching $\sim 3, 4, 1,$ and $0.8 \text{ Mpc } h^{-1}$ in the uniform, scale-invariant, helical, and nonhelical models, respectively). Previous modeling of PMFs in the early universe (in the radiation-dominated epoch) showed the same trend: inflationary, scale-invariant scenarios lead to coherent magnetic structures on larger scales than in the phase-transitional cases (Brandenburg et al. 2017, 2018, 2020). We found that the final magnetic correlation length in the phase-transitional cases is strongly correlated with the initial peak spectrum, limiting the magnetic growth at selected scales of the cosmic web.
5. *Uniform versus stochastic inflationary models.* The late ($z > 6$) evolution of spectral magnetic energy of an inflationary, scale-invariant case at scales $\lesssim 10 \text{ Mpc } h^{-1}$ shows similar amplification as the inflationary uniform case. A uniform, homogeneous seed magnetic field that is customary to use in cosmological MHD simulations is a good representation of a scale-invariant magnetic field on scales smaller than $\sim 29 \text{ Mpc } h^{-1}$ at $z = 0.02$.
6. *Nonhelical versus helical phase-transitional models.* The spectral evolution of the phase-transitional helical and nonhelical models are similar at all wavenumbers. However, the helical model exhibits more amplification as a result of larger initial correlation length and power on a characteristic scale than in the nonhelical scenario. We have shown that, within the limitations of our modeling, it will be hard to distinguish observationally between helical and nonhelical scenarios.
7. *RM predictions.* Significant differences are observed in Faraday rotation measure maps for different PMF models. These differences arise both in the collapsed objects and in the low-density regions of the cosmic web. We computed the rms $|RM|$ excess coming from random redshift pairs ($z \leq 3$) for the regions excluding galaxy clusters and the WHIM. RM values for all the models are lower than expected from the recent observations reported at 144 MHz (O'Sullivan et al. 2020). Our RM analysis favors inflationary seed fields with larger magnetization levels in filamentary structures.
8. *Non-Gaussianity.* We find non-Gaussian trends in the magnetic field PDFs for both inflationary and phase-transitional seedings. This is also imprinted on the distribution functions of the absolute RM, where all models show deviation from a log-normal distribution. The low-end tail (10^{-12} – 10^{-10} G) of the magnetic field PDFs is similar for all models; on the contrary, we observe larger differences between the models in the RM distribution function for both the low- (10^{-8} – 10^{-5} rad m^2) and high-end tails (10^{-1} – 10^2 rad m^2) of the PDFs.

In summary, our results indicate that phase-transitional and inflationary PMFs lead to different realizations of the magnetized cosmic web (retaining the information of magnetic initial conditions on the largest scales of the universe). The differences can potentially be probed observationally. The Faraday rotation measures from our simulations manifest the traces of the initial magnetic seeding. A stronger and more correlated RM signal is expected from inflationary scenarios as a result of larger initial correlation lengths and higher final magnetization levels in filaments from these scenarios. In future work we will complement our analysis by stacking the cosmological boxes and producing light cones to give more realistic estimates of RMs. Future observations (e.g., the SKA) will detect RM signals over a large extent of the sky and have the potential of unraveling the origin of magnetic fields on filamentary scales. Then the results of future work can be readily compared to those observations probing the large-/small-scale nature of the seed magnetic fields.

Finally, future numerical work related to high-energy gamma-ray propagation in cosmic voids (for relevant studies, see, e.g., Dolag et al. 2011, Alves Batista et al. 2017, Vazza et al. 2017, and Bondarenko et al. 2021 for a recent work) will be relevant to probe the seed magnetic fields studied in our work. It is not clear a priori what kind of topology of void

magnetic fields is responsible for the suppression of the secondary gamma-ray flux (Neronov & Vovk 2010). Therefore, studying inflationary and phase-transitional scenarios in the context of the magnetization of cosmic voids could help to more stringently discriminate between the competing magnetogenesis scenarios. This, in turn, will help us understand the effects of such fields on the reionization history of the universe and first structure formation (see, e.g., Koh et al. 2021). Our work gives a first step and a novel approach in the search for the origin of cosmic magnetic fields. Future effort in combining state-of-the-art MHD cosmological simulations and more realistic initial magnetic field conditions will be needed to explore the role of the primordial fields on galaxy-cluster scales and down to smaller scales.

The computations described in this work were performed using the publicly available `Enzo` code (<http://enzo-project.org>), which is the product of a collaborative effort of many independent scientists from numerous institutions around the world. Their commitment to open science has helped make this work possible. We also acknowledge the `yt` toolkit (Turk et al. 2011), which was used as the analysis tool for our project. This work was supported by the Norddeutscher Verbund für Hoch- und Höchstleistungsrechnen (HLRN) under project number: hhp00046 with P.D.F. as principal investigator.

We thank Franco Vazza for sharing the ENZO initial setup and for his comments on the first revision of the manuscript. We appreciate useful discussions and comments from Emma Clarke, Klaus Dolag, Sayan Mandal, Jens Niemeyer, Alberto Roper Pol, and Alexander Tevzadze. S.M. acknowledges the financial support from Shota Rustaveli National Science Foundation of Georgia (SRNSFG, grant No. PHDF_19_4101) and Volkswagen foundation. P.D.F. was supported by the National Research Foundation (NRF) of Korea through grant Nos. 2016R1A5A1013277 and 2020R1A2C2102800. A.B. acknowledges support from the Swedish Research Council (Vetenskapsrådet, grant No. 2019-04234). M.B. acknowledges the financial support from the European Union’s Horizon 2020 program under the ERC Starting Grant “MAGCOW”, grant No. 714196. Finally, we thank the anonymous reviewer for his/her helpful suggestions that improved the quality of this manuscript.

Software: The source codes used for the simulations of this study, ENZO (Brummel-Smith et al. 2019) and the PENCIL CODE (Pencil Code Collaboration et al. 2021), are freely available on <https://github.com/enzo-project/enzo-dev> and <https://github.com/pencil-code/>.

Data Availability

The data underlying this article will be shared on reasonable request to the corresponding author.

Appendix A PENCIL CODE Initial Conditions

We use different initial magnetic fields in our four sets of simulations. First, we use a uniform magnetic field, which was already implemented in the `Enzo` code. Second, a stochastic magnetic field requires a special treatment as it is the result of an MHD simulations with the PENCIL CODE (Pencil Code Collaboration et al. 2021). In this code, we solve the compressible resistive MHD equations (Brandenburg et al. 1996), in which we advanced the magnetic vector potential. We

adopt an ultrarelativistic equation of state, appropriate during the radiation era. The initial condition consists of a Gaussian-distributed spatially random field such that the magnetic energy spectrum has a certain shape: proportional to k^{-1} for the scale-invariant spectrum and proportional to k^4 for wavenumbers $k < k_*$ and proportional to $k^{-5/3}$ for $k > k_*$ in the case of a phase-transitional initial magnetic field. The simulation domain is triply periodic and normalized such that its volume is $(2\pi)^3$, and so the smallest wavenumber in the domain is then $k_1 = 1$. We choose $k_* = 120$ for the runs with phase-transitional initial magnetic fields. The sound speed c_s and the mean density are normalized to unity. The rms magnetic field, and thus the initial rms Alfvén speed, is $v_A = 0.1, \dots, 0.2$. We solve the equations for a time interval Δt such that $c_s k_1 \Delta t = 10$, corresponding to $v_A k_* \Delta t \approx 200$.

We generate the magnetic field components as eigenfunctions of the curl operator, but for helical fields the sign of the eigenvalue is the same for all wavevectors; see Equation (23) of Brandenburg et al. (2017). Helical magnetic fields are still random and isotropic, but they have the same systematic swirl of field lines everywhere in the domain, just like a box with randomly oriented screws which all have the same sense of winding.

The use of a stochastic initial magnetic field requires a modification of `Enzo` where the field is normalized such that for each component $B_{s,i}$, the input (proper) magnetic field is

$$B_{s,i} = \frac{B_p}{\sigma_p} B_{\text{com},i} (1 + z_{\text{ini}})^2, \quad (6)$$

where B_p is the input from the PENCIL CODE, σ_p is its standard deviation, and z_{ini} is the initial redshift ($z = 50$). We set $B_{\text{com},i} = 1$ nG and take $B_{u,i} = \text{RMS}[B_{s,i}]$ for the B -field components in the case of a uniform initial field. In this way, we normalize all the initial conditions to have the same magnetic energy, $\int (\mathbf{B}^2 / 8\pi) dV$.

Appendix B Resolution Tests

In order to test the convergence of our simulations, we compared our setup with the higher-resolution runs including uniform and helical magnetic seeding only (as the evolution of the power spectrum seems to be similar toward smaller scales in the uniform and scale-invariant cases and helical and nonhelical cases). These runs used the same set of cosmological parameters and box size as is used in the main paper. Since the initial stochastic magnetic field distributions are obtained from the PENCIL CODE, in the helical case we used the AMR technique of the `Enzo` code (Bryan et al. 2014) to reach the same resolution ($132 h^{-1}$ kpc) as in the uniform case with 1024^3 grid points. In Figure 12 we show the growth of the magnetic field power spectrum as a function of spatial resolution. As we can see, for our case (i.e., the run with 512^3 grid points, $\Delta x = 132 h^{-1}$ kpc resolution), the magnetic energy in Fourier space for the uniform seeding (solid lines) would be underestimated on scales $\sim k > 0.5 h \text{ Mpc}^{-1}$ (cluster scales), while in the helical case (dashed lines) only a minor difference is expected when doubling the resolution. As we can also see, the larger scales $k \lesssim 0.5 h \text{ Mpc}^{-1}$ are well converged in our simulations.

Conversely, we can see in Figure 13 that the median profiles show no differences in the trends when the higher-resolution simulation is seeded by the uniform magnetic field. On the other

hand, in the case of helical seeding (dashed lines), higher B -field strength is achieved in the filaments' and clusters' regions and lower strengths in the voids for the higher-resolution run. Therefore, we would expect the differences between the inflationary and phase-transitional models to be decreased in these regions as a result of higher resolution.

In Figure 14 we also show the resolution dependence of the PDF of absolute RM. We see that RM values show convergence in the regions where we exclude galaxy clusters, while RMs in galaxy clusters are mostly affected at the high-end and low-end tail of the distribution. This means that our analysis of Section 4.4 will be more affected in galaxy-cluster regions.

Appendix C Testing the Riemann Solver

An important aspect of our work is also to determine the dependencies of our results on the adopted numerical methods. As discussed in Section 4.2, PMFs are expected to heat the IGM at high redshifts. Nevertheless, the absence of heating and cooling physics in our simulations poses a challenge for the interpretation of large thermal energies observed in the turbulent helical and nonhelical models at redshifts $z > 10$ (see Figure 5). In order to check the energy evolution, we have tested our setup with two different Riemann solvers, the LLF and the HLL. Note that the LLF scheme is considerably more diffusive than the HLL scheme. In Figure 15 we show the evolution of thermal, kinetic, and magnetic energies obtained from these two setups. Additionally, we show the evolution of thermal and kinetic energies for a $B = 0$ case using the HLL Riemann solver. As we can see, the pure hydrodynamical setup shows the lowest thermal energy at high redshifts in comparison to the MHD cases. On the other hand, the evolutionary trends of the thermal and kinetic energies in the MHD cases are not affected by the change of Riemann solvers. This shows that the already observed differences between turbulent, nonhelical, and uniform models in thermal energy (see discussion in Section 4.2) are not dependent on the selection of the Riemann solver. However, the LLF scheme substantially affects the evolution of the magnetic energy in the nonhelical case. The stronger numerical diffusion completely suppresses the magnetic field amplification at lower redshifts, suggesting that this method may not be optimal for the study of stochastic PMFs.

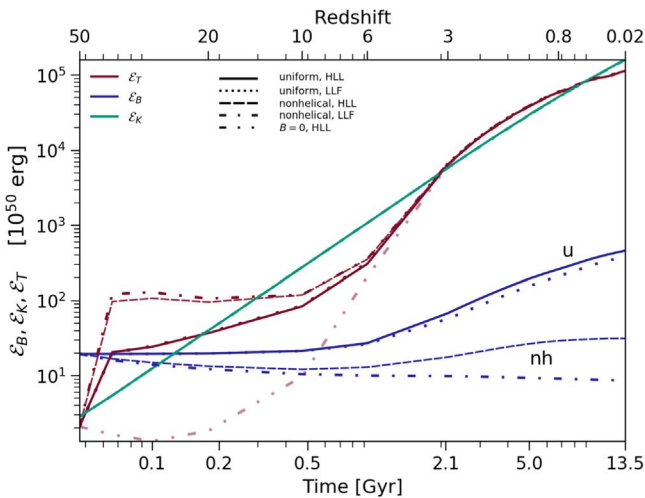


Figure 15. Evolution of magnetic, thermal, and kinetic energies for the uniform and nonhelical cases when using HLL (solid, dashed, dashed-dotted lines, where the latter corresponds to the $B = 0$ case) and LLF (dotted and dashed-dotted lines) Riemann solver schemes.

Appendix D Tangling of a Homogeneous Field

In Section 4.3, we noted the rather different response to an imposed (uniform) magnetic field in the present simulations (see the first panel of Figure 6) and those of Brandenburg et al. (2020), where magnetic fields at the scale of the domain began to grow only after smaller-scale magnetic fields have grown first. An important difference, however, is that our present cosmological simulations always possess a large-scale velocity field, which was not present in the simulations of Brandenburg et al. (2020). The large-scale velocity field in the cosmological simulations leads to tangling of the uniform imposed magnetic field, which leads to the instantaneous growth immediately at the beginning of the simulation.

To verify our reasoning above, we now repeat the simulations presented in Figure 5 of Brandenburg et al. (2020) with a weak imposed field, but now with a random initial velocity field with an initial kinetic energy spectrum proportional to k^{-2} . The result is shown in Figure 16, where we show the resulting magnetic and kinetic energy spectra. Note the increase of spectral magnetic energy at all wavenumbers already occurs from early times onwards. This is caused by the tangling of the homogeneous magnetic field by the initial large-scale velocity field with a k^{-2} spectrum. This therefore confirms our reasoning in Section 4.3 concerning the rather different response to an imposed magnetic field in the present simulations and those of Brandenburg et al. (2020).

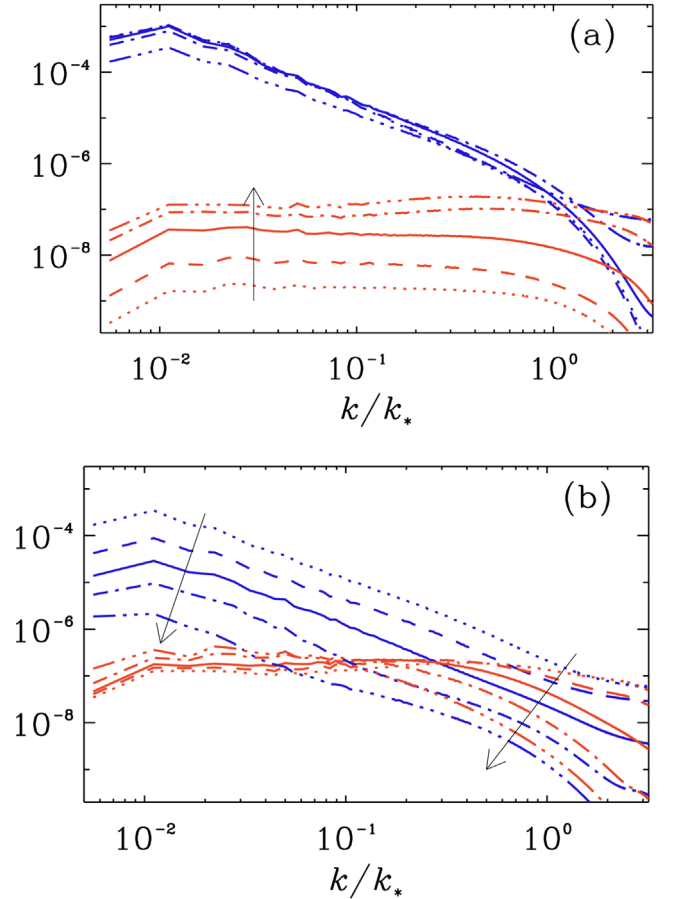


Figure 16. MHD simulations with an initial kinetic energy spectrum proportional to k^{-2} in the presence of a weak homogeneous magnetic field. Panels (a) and (b) show the early and late evolution for magnetic energy spectra (red) and kinetic energy spectra (blue).

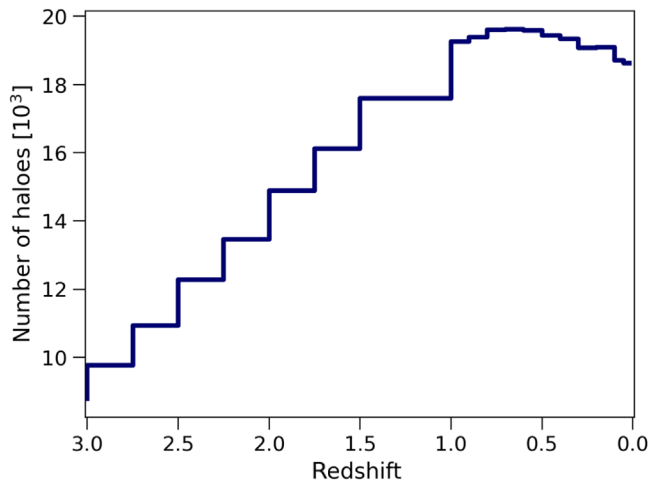


Figure 17. Number of virialized objects with baryonic mass range $10^7 M_{\odot} \leq M \leq 10^{10} M_{\odot}$ as function of redshift. The masses have been calculated within the sphere enclosing the virial radius of each source. This radius is an output of the *yt* halo finder.

Appendix E RM Sources

As we mentioned in Section 4.4, our statistical RM analysis does not take into account the spatial distribution of sources at each redshift. Nevertheless, we show the expected redshift distribution of sources in Figure 17 for completeness. For this figure, we used the *yt* halo finder (Skory et al. 2011), which identifies the groups of linked DM particles based on the Eisenstein & Hut (1998) algorithm, for each redshift in order to find a selected number of haloes with a baryonic mass range $10^7 M_{\odot} \leq M \leq 10^{10} M_{\odot}$. This range resembles the masses of FR II galaxies, which are the typical type of polarized sources found in large catalogs (e.g., Taylor et al. 2009; Van Eck et al. 2018).

ORCID iDs

Salome Mtchedlidze <https://orcid.org/0000-0001-9786-8882>
 Paola Domínguez-Fernández <https://orcid.org/0000-0001-7058-8418>
 Xiaolong Du <https://orcid.org/0000-0003-0728-2533>
 Axel Brandenburg <https://orcid.org/0000-0002-7304-021X>
 Tina Kahniashvili <https://orcid.org/0000-0003-0217-9852>
 Shane O’Sullivan <https://orcid.org/0000-0002-3968-3051>
 Wolfram Schmidt <https://orcid.org/0000-0001-5233-8087>
 Marcus Brüggen <https://orcid.org/0000-0002-3369-7735>

References

Ade, P. A. R., Arnold, K., Atlas, M., et al. 2015, *PhRvD*, **92**, 123509
 Akahori, T., & Ryu, D. 2010, *ApJ*, **723**, 476
 Akahori, T., & Ryu, D. 2011, *ApJ*, **738**, 134
 Alves Batista, R., Saveliev, A., & de Gouveia Dal Pino, E. M. 2019, *MNRAS*, **489**, 3836
 Alves Batista, R., Shin, M.-S., Devriendt, J., Semikoz, D., & Sigl, G. 2017, *PhRvD*, **96**, 023010
 Arámburo-García, A., Bondarenko, K., Boyarsky, A., et al. 2021, *MNRAS*, **505**, 5038
 Arlen, T. C., Vassiliev, V. V., Weisgarber, T., Wakely, S. P., & Shafi, S. Y. 2014, *ApJ*, **796**, 18
 Attia, O., Teyssier, R., Katz, H., et al. 2021, *MNRAS*, **504**, 2346
 Bamba, K., Elizalde, E., Odintsov, S. D., & Paul, T. 2021, *JCAP*, **2021**, 009

Banerjee, R., & Jedamzik, K. 2004, *PhRvD*, **70**, 123003
 Barkana, R. 2018, *Natur*, **555**, 71
 Barnes, D. J., On, A. Y. L., Wu, K., & Kawata, D. 2018, *MNRAS*, **476**, 2890
 Beck, R. 2001, *SSRv*, **99**, 243
 Beck, R., & Wielebinski, R. 2013, in Planets, Stars and Stellar Systems, ed. T. D. Oswalt & G. Gilmore, Vol. 5 (Dordrecht: Springer), 641
 Bera, A., Datta, K. K., & Samui, S. 2020, *MNRAS*, **498**, 918
 Beresnyak, A., & Miniati, F. 2016, *ApJ*, **817**, 127
 Bernet, M. L., Miniati, F., & Lilly, S. J. 2010, *ApJ*, **711**, 380
 Bernet, M. L., Miniati, F., Lilly, S. J., Kronberg, P. P., & Dessauges-Zavadsky, M. 2008, *Natur*, **454**, 302
 Bertone, S., Vogt, C., & Enßlin, T. 2006, *MNRAS*, **370**, 319
 Biermann, L. 1950, *ZNatA*, **5**, 65
 Böhringer, H., Chon, G., & Kronberg, P. P. 2016, *A&A*, **596**, A22
 Bondarenko, K., Boyarsky, A., Korochkin, A., et al. 2021, arXiv:2106.02690
 Bowman, J. D., Rogers, A. E. E., Monsalve, R. A., Mozdzen, T. J., & Mahesh, N. 2018, *Natur*, **555**, 67
 Brandenburg, A., Durrer, R., Huang, Y., et al. 2020, *PhRvD*, **102**, 023536
 Brandenburg, A., Durrer, R., Kahniashvili, T., Mandal, S., & Yin, W. W. 2018, *JCAP*, **2018**, 034
 Brandenburg, A., Enqvist, K., & Olesen, P. 1996, *PhRvD*, **54**, 1291
 Brandenburg, A., & Kahniashvili, T. 2017, *PhRvL*, **118**, 055102
 Brandenburg, A., Kahniashvili, T., Mandal, S., et al. 2017, *PhRvD*, **96**, 123528
 Brandenburg, A., Kahniashvili, T., & Tevzadze, A. G. 2015, *PhRvL*, **114**, 075001
 Brandenburg, A., & Nordlund, Å. 2011, *RPPH*, **74**, 046901
 Braun, R. 2015, *IAUGA*, **29**, 2252814
 Broderick, A. E., Tiede, P., Chang, P., et al. 2018, *ApJ*, **868**, 87
 Brüggén, M., Ruszkowski, M., Simionescu, A., Hoeft, M., & Dalla Vecchia, C. 2005, *ApJL*, **631**, L21
 Brummel-Smith, C., Bryan, G., Butsky, I., et al. 2019, *JOSS*, **4**, 1636
 Bryan, G. L., Norman, M. L., Stone, J. M., Cen, R., & Ostriker, J. P. 1995, *CoPhC*, **89**, 149
 Bryan, G. L., Norman, M. L., O’Shea, B. W., et al. 2014, *ApJS*, **211**, 19
 Burn, B. J. 1966, *MNRAS*, **133**, 67
 Cho, J. 2014, *ApJ*, **797**, 133
 Christensson, M., Hindmarsh, M., & Brandenburg, A. 2001, *PhRvE*, **64**, 056405
 Colella, P., & Glaz, H. M. 1985, *JCoPh*, **59**, 264
 Cornwall, J. M. 1997, *PhRvD*, **56**, 6146
 de Bruyn, A. G., & Brentjens, M. A. 2005, *A&A*, **441**, 931
 Dedner, A., Kemm, F., Kröner, D., et al. 2002, *JCoPh*, **175**, 645
 Dolag, K., Bartelmann, M., & Lesch, H. 1999, arXiv:astro-ph/9906329
 Dolag, K., Kachelriess, M., Ostapchenko, S., & Tomàs, R. 2011, *ApJL*, **727**, L4
 Dolgov, A. D. 1993, *PhRvD*, **48**, 2499
 Domínguez-Fernández, P., Vazza, F., Brüggén, M., & Brunetti, G. 2019, *MNRAS*, **486**, 623
 Donnert, J., Dolag, K., Lesch, H., & Müller, E. 2009, *MNRAS*, **392**, 1008
 Donnert, J., Vazza, F., Brüggén, M., & ZuHone, J. 2018, *SSRv*, **214**, 122
 Dubois, Y., & Teyssier, R. 2008, *A&A*, **482**, L13
 Durrer, R., & Caprini, C. 2003, *JCAP*, **2003**, 010
 Durrer, R., Kunz, M., & Melchiorri, A. 2002, *PhR*, **364**, 1
 Durrer, R., & Neronov, A. 2013, *A&ARv*, **21**, 62
 Eisenstein, D. J., & Hu, W. 1998, *ApJ*, **496**, 605
 Eisenstein, D. J., & Hut, P. 1998, *ApJ*, **498**, 137
 Fedeli, C., & Moscardini, L. 2012, *JCAP*, **2012**, 055
 Fujita, T., & Kamada, K. 2016, *PhRvD*, **93**, 083520
 Fusco-Femiano, R., Dal Fiume, D., Orlandini, M., et al. 2001, *ApJL*, **552**, L97
 Fusco-Femiano, R., Orlandini, M., Brunetti, G., et al. 2004, *ApJL*, **602**, L73
 Galli, S., Pogosian, L., Jedamzik, K., & Balkenhol, L. 2022, *PhRvD*, **105**, 023513
 Garaldi, E., Pakmor, R., & Springel, V. 2021, *MNRAS*, **502**, 5726
 Gheller, C., & Vazza, F. 2019, *MNRAS*, **486**, 981
 Giovannini, M., & Shaposhnikov, M. E. 1998, *PhRvL*, **80**, 22
 Gnedin, N. Y. 2000, *ApJ*, **542**, 535
 Gopal, R., & Sethi, S. K. 2003, *JApA*, **24**, 51
 Govoni, F., Orrù, E., Bonafede, A., et al. 2019, *Sci*, **364**, 981
 Grasso, D., & Rubinstein, H. R. 2001, *PhR*, **348**, 163
 Hahn, O., & Abel, T. 2011, *MNRAS*, **415**, 2101
 Hogan, C. J. 1983, *PhRvL*, **51**, 1488
 Hopkins, P. F., & Raives, M. J. 2016, *MNRAS*, **455**, 51
 Horiguchi, K., Ichiki, K., Sekiguchi, T., & Sugiyama, N. 2015, *JCAP*, **2015**, 007
 Hutschenreuter, S., Anderson, C. S., Betti, S., et al. 2021, *A&A*, **657**, 43

- Jedamzik, K., Katalinić, V., & Olinto, A. V. 1998, *PhRvD*, **57**, 3264
- Jedamzik, K., Katalinić, V. c. v., & Olinto, A. V. 2000, *PhRvL*, **85**, 700
- Jedamzik, K., & Pogosian, L. 2020, *PhRvL*, **125**, 181302
- Jedamzik, K., & Saveliev, A. 2019, *PhRvL*, **123**, 021301
- Kahniashvili, T., Brandenburg, A., Durrer, R., Tevzadze, A. G., & Yin, W. 2017, *JCAP*, **2017**, 002
- Kahniashvili, T., Brandenburg, A., Gogoberidze, G., Mandal, S., & Roper Pol, A. 2021, *PhRvR*, **3**, 013193
- Kahniashvili, T., Brandenburg, A., Kosowsky, A., Mandal, S., & Roper Pol, A. 2020, *IAUGA*, **30**, 295
- Kahniashvili, T., Brandenburg, A., & Tevzadze, A. e. G. 2016, *PhysS*, **91**, 104008
- Kahniashvili, T., Brandenburg, A., Tevzadze, A. e. G., & Ratra, B. 2010, *PhRvD*, **81**, 123002
- Kahniashvili, T., Maravin, Y., Natarajan, A., Battaglia, N., & Tevzadze, A. G. 2013, *ApJ*, **770**, 47
- Kandus, A., Kunze, K. E., & Tsagas, C. G. 2011, *PhR*, **505**, 1
- Katz, H., Martin-Alvarez, S., Rosdahl, J., et al. 2021, *MNRAS*, **507**, 1254
- Kim, E.-J., Olinto, A. V., & Rosner, R. 1996, *ApJ*, **468**, 28
- Koh, D., Abel, T., & Jedamzik, K. 2021, *ApJL*, **909**, L21
- Kritsuk, A. G., Nordlund, Å., Collins, D., et al. 2011, *ApJ*, **737**, 13
- Kronberg, P. P., Bernet, M. L., Miniati, F., et al. 2008, *ApJ*, **676**, 70
- Kulsrud, R. M., & Zweibel, E. G. 2008, *RPPH*, **71**, 0046091
- Kurganov, A., & Tadmor, E. 2000, *JCoPh*, **160**, 241
- Kushwaha, A., & Shankaranarayanan, S. 2021, *PhRvD*, **104**, 063502
- Luo, Y., Kajino, T., Kusakabe, M., & Mathews, G. J. 2019, *ApJ*, **872**, 172
- Maity, D., Pal, S., & Paul, T. 2021, *JCAP*, **2021**, 045
- Marinacci, F., Vogelsberger, M., Mocz, P., & Pakmor, R. 2015, *MNRAS*, **453**, 3999
- Marinacci, F., Vogelsberger, M., Pakmor, R., et al. 2018, *MNRAS*, **480**, 5113
- Minami, Y., & Komatsu, E. 2020, *PhRvL*, **125**, 221301
- Miniati, F., & Beresnyak, A. 2015, *Natur*, **523**, 59
- Minoda, T., Hasegawa, K., Tashiro, H., Ichiki, K., & Sugiyama, N. 2017, *PhRvD*, **96**, 123525
- Minoda, T., Tashiro, H., & Takahashi, T. 2019, *MNRAS*, **488**, 2001
- Mukohyama, S. 2016, *PhRvD*, **94**, 121302
- Murgia, M., Govoni, F., Ferretti, L., et al. 2004, *A&A*, **424**, 429
- Naos, S., & Narayan, R. 2013, *PhRvL*, **111**, 051303
- Natwariya, P. K. 2021, *EPJC*, **81**, 394
- Neronov, A., & Vovk, I. 2010, *Sci*, **328**, 73
- Oppermann, N., Junklewitz, H., Greiner, M., et al. 2015, *A&A*, **575**, A118
- O'Sullivan, S. P., Brügger, M., Vazza, F., et al. 2020, *MNRAS*, **495**, 2607
- Pakmor, R., Marinacci, F., & Springel, V. 2014, *ApJL*, **783**, L20
- Pakmor, R., Gómez, F. A., Grand, R. J. J., et al. 2017, *MNRAS*, **469**, 3185
- Pandey, K. L., Sethi, S. K., & Ratra, B. 2019, *MNRAS*, **486**, 1629
- Pencil Code Collaboration, Brandenburg, A., Johansen, A., et al. 2021, *JOSS*, **6**, 2807
- Pillepich, A., Springel, V., Nelson, D., et al. 2018, *MNRAS*, **473**, 4077
- Planck Collaboration, Ade, P. A. R., Aghanim, N., et al. 2016, *A&A*, **594**, A19
- Planck Collaboration, Aghanim, N., Akrami, Y., et al. 2020, *A&A*, **641**, A6
- Pouquet, A., Frisch, U., & Léorat, J. 1976, *JFM*, **77**, 321
- Quashnock, J. M., Loeb, A., & Spergel, D. N. 1989, *ApJL*, **344**, L49
- Ratra, B. 1992, *ApJL*, **391**, L1
- Reiprich, T. H., Veronica, A., Pacaud, F., et al. 2021, *A&A*, **647**, A2
- Rieder, M., & Teysier, R. 2017, *MNRAS*, **471**, 2674
- Ryu, D., Kang, H., & Biermann, P. L. 1998, *A&A*, **335**, 19
- Ryu, D., Kang, H., Cho, J., & Das, S. 2008, *Sci*, **320**, 909
- Sanati, M., Revaz, Y., Schober, J., Kunze, K. E., & Jablonka, P. 2020, *A&A*, **643**, A54
- Scaramella, R., Cen, R., & Ostriker, J. P. 1993, *ApJ*, **416**, 399
- Schekochihin, A., Cowley, S., Hammett, G., et al. 2004, APS Meeting, **46**, JO2.008
- Schnitzeler, D. H. F. M. 2010, *MNRAS*, **409**, L99
- Schubert, G., & Soderlund, K. M. 2011, *PEPI*, **187**, 92
- Schwarz, D. J. 2003, *AnP*, **12**, 220
- Seta, A., & Federrath, C. 2020, *MNRAS*, **499**, 2076
- Seta, A., Shukurov, A., Wood, T. S., Bushby, P. J., & Snodin, A. P. 2018, *MNRAS*, **473**, 4544
- Sethi, S. K. 2005, *MNRAS*, **363**, 818
- Sethi, S. K., & Subramanian, K. 2005, *MNRAS*, **356**, 778
- Sethi, S. K., & Subramanian, K. 2009, *JCAP*, **2009**, 021
- Sharma, R., Jagannathan, S., Seshadri, T. R., & Subramanian, K. 2017, *PhRvD*, **96**, 083511
- Sharma, R., Subramanian, K., & Seshadri, T. R. 2018, *PhRvD*, **97**, 083503
- Shimwell, T. W., Tasse, C., Hardcastle, M. J., et al. 2019, *A&A*, **622**, A1
- Shu, C.-W., & Osher, S. 1988, *JCoPh*, **77**, 439
- Skory, S., Turk, M. J., Norman, M. L., & Coil, A. L. 2011, Parallel HOP: A Scalable Halo Finder for Massive Cosmological Data Sets, Astrophysics Source Code Library, ascl:1103.008
- Smith, D. J. B., Best, P. N., Duncan, K. J., et al. 2016, in SF2A-2016: Proc. of the Annual meeting of the French Society of Astronomy and Astrophysics, ed. C. Reylé et al.
- Sotomayor-Beltran, C., Sobey, C., Hessels, J. W. T., et al. 2013, *A&A*, **552**, A58
- Steinwandel, U. P., Boess, L. M., Dolag, K., & Lesch, H. 2021, arXiv:2108.07822
- Steinwandel, U. P., Dolag, K., Lesch, H., et al. 2020, *MNRAS*, **494**, 4393
- Stevenson, D. J. 2010, *SSRv*, **152**, 651
- Stuardi, C., O'Sullivan, S. P., Bonafede, A., et al. 2020, *A&A*, **638**, A48
- Subramanian, K. 2016, *RPPH*, **79**, 076901
- Subramanian, K., Narasimha, D., & Chitre, S. M. 1994, *MNRAS*, **271**, L15
- Tajima, T., Cable, S., Shibata, K., & Kulsrud, R. M. 1992, *ApJ*, **390**, 309
- Tavecchio, F., Ghisellini, G., Foschini, L., et al. 2010, *MNRAS*, **406**, L70
- Taylor, A. M., Vovk, I., & Neronov, A. 2011, *A&A*, **529**, A144
- Taylor, A. R., Stil, J. M., & Sunstrum, C. 2009, *ApJ*, **702**, 1230
- Thomas, P., & Carlberg, R. G. 1989, *MNRAS*, **240**, 1009
- Toro, E. F. 1997, The HLL and HLLC Riemann Solvers (Berlin: Springer), 293
- Tricco, T. S., Price, D. J., & Federrath, C. 2016, *MNRAS*, **461**, 1260
- Turk, M. J., Smith, B. D., Oishi, J. S., et al. 2011, *ApJS*, **192**, 9
- Turner, M. S., & Widrow, L. M. 1988, *PhRvD*, **37**, 2743
- Vachaspati, T. 1991, *PhLB*, **265**, 258
- Vachaspati, T. 2001, *PhRvL*, **87**, 251302
- Vachaspati, T. 2021, *RPPH*, **84**, 074901
- Väisälä, M. S., Pekkilä, J., Käpylä, M. J., et al. 2021, *ApJ*, **907**, 83
- Van Eck, C. L., Haverkorn, M., Alves, M. I. R., et al. 2018, *A&A*, **613**, A58
- van Leer, B. 1979, *JCoPh*, **32**, 101
- Vazza, F., Brügger, M., Gheller, C., et al. 2017, *CQGra*, **34**, 234001
- Vazza, F., Brügger, M., Gheller, C., & Wang, P. 2014, *MNRAS*, **445**, 3706
- Vazza, F., Brunetti, G., Brügger, M., & Bonafede, A. 2018, *MNRAS*, **474**, 1672
- Vazza, F., Paoletti, D., Banfi, S., et al. 2021, *MNRAS*, **500**, 5350
- Vernstrom, T., Gaensler, B. M., Rudnick, L., & Andernach, H. 2019, *ApJ*, **878**, 92
- Vogt, C., & Enßlin, T. A. 2005, *A&A*, **434**, 67
- Wang, P., & Abel, T. 2009, *ApJ*, **696**, 96
- Wang, P., Abel, T., & Kaehler, R. 2010, *NewA*, **15**, 581
- Wasserman, I. 1978, *ApJ*, **224**, 337
- Xu, H., Li, H., Collins, D. C., Li, S., & Norman, M. L. 2009, *ApJL*, **698**, L14
- Xu, H., Li, H., Collins, D. C., Li, S., & Norman, M. L. 2011, *ApJ*, **739**, 77
- Yamazaki, D. G., Ichiki, K., Umezu, K.-I., & Hanayama, H. 2006, *PhRvD*, **74**, 123518
- Yamazaki, D. G., & Kusakabe, M. 2012, *PhRvD*, **86**, 123006